Intra-annual grounding-line migration and retreat: insights from high-resolution satellite and in situ observations over Milne Glacier in the Canadian High Arctic

Yulia K. Antropova[1], Derek Mueller[1], Sergey V. Samsonov[2], Alexander S. Komarov[3], Jérémie Bonneau[4,5]

[1]Department of Geography and Environmental Studies, Carleton University, Ottawa, K1S 5B6, Canada
[2]Canadian Centre for Mapping and Earth Observations, Natural Resources Canada, Ottawa, K1A 0E4, Canada
[3]Earth System Research and Integration Division, Environment and Climate Change Canada, Ottawa, K1A 0H3, Canada
[4]Department of Civil Engineering, The University of British Columbia, Vancouver, V6T 1Z2, Canada
[5]Département de Génie Civil et Génie des Eaux, Université Laval, Québec, G1V 0A6, Canada

Correspondence to: Yulia K. Antropova (YuliaAntropova@cmail.carleton.ca)

Abstract. Monitoring changes in the position of the boundary where marine-terminating glaciers transition from grounded to floating, known as the grounding line, is critical for advancing our understanding of glacier stability. The grounding line is difficult to observe directly but can be inferred from the ice surface tidal-flexure zone. This zone spans from the inland limit of tidal flexure ─ the hinge line, across the grounding line to the hydrostatic line, where the glacier becomes freely floating. We explore flexure zone changes on Milne Glacier, Nunavut, Canada from 2023 to 2024 at a high spatial resolution of 10 m using 4-day RADARSAT Constellation Mission (RCM) data acquisitions from four different orbits. The Double Difference Interferometric Synthetic Aperture Radar (DDInSAR) technique was employed to delineate 116 flexure zones through time, which were then examined with respect to SAR viewing geometry, tides and atmospheric pressure variability, glacier velocity changes, and ice bending, as well as ice surface and bed topography. The most reliable flexure zone delineation (horizontal uncertainty of ±8 m) was achieved with ascending RCM tracks at low incidence angles during periods when the ice velocity was steady and bending was not substantial, resulting in a combined SAR line-of-sight error of 0.13 cm. A worst-case flexure-zone delineation uncertainty of ±222 m was noted when a descending track with a high incidence angle was used and glacier velocity became more variable, increasing the combined SAR line-of-sight error to 3.26 cm. Low-error DDInSAR images enabled the detection of a newly developed ~2.4 km grounding-line retreat associated with the emergence of a new pinning point at the eastern margin of the glacier. Our results underscore that care must be taken to ensure that the low-error DDInSAR results are used when monitoring changes in grounding-line position and that pinning points alter the grounding-line short-term migration and its long-term retreat.

1. Introduction

Marine-terminating glaciers, which drain ice masses from land to the ocean, have experienced dramatic changes in recent decades due to a warming climate, particularly in the Arctic, where temperatures are rising faster than the global average

(Black & Joughin, 2022; Kochtitzky & Copland, 2022; Rantanen et al., 2022). Rising atmospheric and oceanic temperatures can cause these glaciers to accelerate, leading to increased sea level rise and discharge of icebergs or ice islands into adjacent waters (Morlighem et al., 2019; Wood et al., 2021; Carnahan et al., 2022; Holmes et al., 2025). Increased ice discharge and ice mass losses associated with Arctic glacier volume decrease, retreat, and deterioration were recently documented by Millan et al. (2017, 2023) and Van Wychen et al. (2020). As a result of these changes, many glaciers located in Greenland and the Canadian Arctic shifted from marine to land-terminating glaciers between 2000 and 2020 (Kochtitzky & Copland, 2022). To characterize and explore the stability of marine terminating glaciers, recent studies have focused on the boundary where glaciers transition from grounded to floating (e.g., Rignot et al., 2024; Kim et al., 2024), known as the grounding line. The grounding line exhibits dynamic behaviour, migrating with tides over short time scales (Freer et al., 2023) and advancing or retreating in response to changes in glacier dynamics over the long term (Milillo et al., 2022; Chartrand et al., 2024). Accurate mapping and monitoring of grounding-line dynamics are crucial for better understanding glacier retreat patterns and the processes that drive this retreat.

The satellite-based Double Difference Interferometric Synthetic Aperture Radar (DDInSAR) method has been proven to be highly effective for accurate monitoring of grounding-line migration, using SAR imagery with high temporal (1-6 days) and spatial (1 m to a few metres) resolution, along with consistent multi-temporal coverage over large areas ranging from tens to several hundreds of kilometres (Rignot et al., 2011; Milillo et al., 2017). This method is based on computing interferograms with the topographic phase removed to reveal surface displacement, followed by differencing two interferograms to eliminate the horizontal ice-flow component of displacement and isolate the vertical displacement associated with tidal forcing (Rignot, 1996). Although different terms have been used to describe this technique, including DInSAR (Rignot et al., 2011; Wild et al., 2025) and quadruple-difference interferometry (Rignot, 1996; Rignot et al., 2014), hereafter we refer to this method as DDInSAR, consistent with Han and Lee (2014) and Antropova et al. (2024), and equivalent to double-difference interferometry (Chen et al., 2023; Andersen et al., 2026). Among the currently operational SAR missions explored for DDInSAR grounding-line applications, the RADARSAT Constellation Mission (RCM, C-band) has a 4-day acquisition cycle (Antropova et al., 2024; Gadi et al., 2025). This is comparable to COSMO-SkyMed (X-band) allowing 1 to 4 day revisits (Milillo et al., 2022; Rignot et al., 2024), and shorter than Sentinel-1 (C-band) with 6 to 12 day revisits (shorter with the A+B or A+C constellations) (Ramanath et al., 2025; Wild et al., 2025), TerraSAR-X (X-band) providing 11-day revisit (shorter with TanDEM-X) (Wild et al., 2018; Wild et al., 2025), and ALOS PALSAR (L-band) with a 46-day revisit (Rignot et al., 2011). The comparatively short revisit time of RCM enables high phase coherence, while its C-band wavelength provides sensitivity to small vertical displacements, allowing reliable DDInSAR measurements for grounding-line monitoring of relatively fast-moving glaciers.

The DDInSAR method detects the differential tidal-flexure zone, hereafter referred to as the flexure zone, where the glacier surface flexure with tides is captured at SAR data acquisition times. This zone, also referred to as the grounding zone in some studies (e.g., Fricker et al., 2009; Freer et al., 2023), spans from the inland limit of tidal flexure (i.e., the hinge line) past the grounding line to the seaward limit of flexure (i.e., hydrostatic line), where hydrostatic equilibrium is reached and the glacier becomes completely buoyant. Nevertheless, most recent DDInSAR-based studies consider the hinge line as a proxy for the

grounding line, so they tend to refer to the hinge line, and the bounds where it migrates over the tidal cycle, as the grounding line and grounding zone, respectively (Mohajerani et al., 2021; Chen et al., 2023; Ciracì et al., 2023; Rignot et al., 2024). To ensure clarity and consistency, hereafter, we use the terms 'flexure-zone width' (i.e., the along-glacier distance from the hinge line to the hydrostatic line) and 'grounding-zone width' (i.e., the along-glacier distance from the most landward hinge line to the most seaward hinge line); to conform with recent DDInSAR studies. We also assume that the relative movements (e.g., short-term migration and long-term retreat) of the DDInSAR-derived 'hinge line' and the actual 'grounding line' are equivalent, as their positions are strongly correlated (Rignot, 1996).

Recent DDInSAR-based studies highlighted the complexity of grounding-line migration with tidal cycles and explored the causes of this complexity, including glacier geometry, underlying bed type, subglacial hydrology, and sea water intrusions (e.g., Mohajerani et al., 2021; Ciracì et al., 2023, Rignot et al., 2024; Kim et al., 2024), as well as the contributions of compressional and tensional strain components induced by ice-surface bending to the DDInSAR signal (Rack et al., 2017; Wild et al., 2018). In addition, DDInSAR-based observations showed that grounding-zone width tends to be one to two orders of magnitude larger than predicted assuming hydrostatic equilibrium (Chen et al., 2023, Milillo et al., 2022, Mohajerani et al., 2021). Since grounding zones are associated with pronounced ice melt, this implies that the assumption that grounding lines are fixed over space and time made by many conventional numerical glacier/ice sheet models is problematic (Ciracì et al., 2023; Rignot et al., 2024). To improve these models, a detailed investigation of the drivers and glacier-system responses governing grounding-line migration over short-term cycles and its long-term advance or retreat is required. The reliability of satellite-based observations used to monitor these processes should also be thoroughly evaluated. Our study explores intra-annual changes in the Milne Glacier flexure zone based on a combination of RCM DDInSAR-derived results, in situ and simulated datasets, and a numerical weather prediction model output. The objectives of this study are to:

- Delineate the Milne Glacier flexure zone using RCM data acquisitions from four different orbits, with a 4-day repeat interval within each orbit and about a 1-day interval between orbits, spanning from February 17, 2023 to September 17, 2024;
- Examine the relationship between DDInSAR-derived ice-surface vertical displacement and differential displacement of sea surface height (DSSH), computed from simulated tides and in situ atmospheric pressure records together with modeled atmospheric pressure. We further assess this correlation across the four SAR orbits with respect to the compressional and tensional strains caused by ice-surface bending in the flexure zone during two velocity periods:

  a) a steady period, when in situ-measured Milne Glacier velocity did not change appreciably during winter and the DDInSAR assumption of invariant velocities was met; and

  b) an unsteady period, when in-situ measured velocity changes were evident, the glacier decelerated after summer peak velocity, and the DDInSAR assumption of invariant velocities was violated;
- Explore flexure-zone changes, including its width, its landward position (i.e., hinge line), and the width of the grounding zone over the study period with respect to DDInSAR-derived surface displacements and glacier surface and bed geometry datasets.

- Test the hypothesis that a newly emerging pinning point along the eastern margin results from inland seawater intrusion driven by high sea-surface height (SSH).

Our results provide insight into short-term migration patterns of the grounding line based on its DDInSAR-derived proxy, the hinge line, and help elucidate the processes that drive long-term grounding-line retreat. By comparing steady and unsteady velocity periods, this study evaluates the reliability of DDInSAR under varying flow conditions and offers new insight into how short-term glacier dynamics influence the interpretation of grounding-line positions derived from high-resolution multi-orbit RCM SAR imagery.

2 Study site and methods

2.1 Study site description

Milne Glacier is located on the northern coast of Ellesmere Island, the largest and northernmost island in the Canadian Arctic Archipelago (Fig. 1 inset map). The glacier is one of the major outlet glaciers of the 'Northern Ellesmere Icefield' (Millan et al., 2017) that discharges terrestrial ice into Milne Fiord. In the past, Milne Glacier was the central and most important glacier feeding the Milne Ice Shelf, the second largest remnant of the extensive Ellesmere Ice Shelf that collapsed in the early 20th Century (Mueller et al., 2017). The separation of Milne Glacier from the Milne Ice Shelf was accompanied by the formation and development of an epishelf lake (i.e., a layer of freshwater from summer ice melt and runoff that accumulates above seawater between the shore and an ice shelf) first reported by Jeffries (1984). The area of thin epishelf lake ice replacing the thick ice shelf increased from 5 km^2 to 17 km^2 between 1959 and 1984, reaching 28.5 km^2 by 2009 (Mortimer et al., 2012; Mueller et al., 2017). Currently, perennial epishelf lake ice and fragments of the former Milne Glacier ice tongue that broke off the glacier between 2009 and 2011 are present within the ~22 km stretch between the present-day floating ice tongue and the ice shelf (Fig. 1 a).

The present-day intact floating ice tongue, located deep within Milne Fiord, is protected from drifting ice along the northern coast of Ellesmere Island (Mortimer et al., 2012). Milne Fiord is characterized by a semi-diurnal tidal regime with a relatively small tidal range, spanning from –20 cm to 21 cm over the observation period of this study, and a 14.8-day spring-neap-spring tidal cycle. However, atmospheric pressure variability also plays an important role in modulating the tidal forcing (Wunsch & Stammer, 1997; Padman et al., 2003), further affecting the vertical displacement of the ice tongue and increasing the flexural stresses it experiences.

The glacier's transition zone between grounded ice and the floating ice tongue exhibited notable velocity fluctuations over the past decades. Ice velocity decreased from ~190 m yr^{-1} to ~100 m yr^{-1} between the 1990s and 2005 (Millan et al., 2017), increased to 120 - 140 m yr^{-1} in 2010, slowed down again to 80 - 100 m yr^{-1} from 2011 to 2015, and then accelerated to 140 - 160 m yr^{-1} between 2016 and 2020 (Van Wychen et al., 2020). Van Wychen et al. (2020) suggested that this cyclical behaviour may result from prominent bedrock features that modulate velocity where the glacier rests below sea level. In addition, Antropova et al. (2024) noted that the post-2016 acceleration was preceded by the highest average grounding-line retreat rate

of 89 m yr^{-1} along the glacier's centreline between 2011 and 2018, suggesting the presence of feedback mechanisms between grounding-line retreat and glacier acceleration.

The Milne Glacier grounding-line retreated by 3.1 km along the glacier's centreline from 1966 to 2023. The average rate of the grounding-line retreat was more than twice as high near the western margin (124 m yr^{-1}) compared to the centre (53 m yr^{-1}) of the glacier between 2011 and 2023. Warming oceanic masses likely enhanced the grounding-line retreat in recent decades since variations in the grounding-line retreat rates were associated with changes in oceanic forcing (Antropova et al., 2024). Vertical thinning due to basal melt, was estimated at 15-32 m yr^{-1} between 2011 and 2019 (Bonneau et al., 2024a) with a greater thinning rate near the glacier's deeper western side than at the shallower central and eastern edges. The glacier's vulnerability to oceanic warming is likely due to its bed geometry (Antropova et al., 2024). Milne Glacier's retrograde bed slope near the present-day grounding line makes the glacier susceptible to marine ice-sheet instability (Weertman, 1974; Schoof, 2007), a process where grounding-line retreat enhances glacier deterioration, which, in turn, triggers further retreat. This positive feedback loop may be underway currently and is expected to persist until the grounding line reaches a prograde bed slope roughly 1 km up-glacier. Based on the glacier's 2011-2023 average retreat rate, this would occur in 2035. However, grounding-line retreat is inherently non-linear and governed by the complex interplay of glacier-specific and environmental controls. Reaching this slope could help stabilize the glacier and inhibit further recession of its grounding line.

2.2 Data and methods

2.2.1 Processing of SAR data

We used RCM single look complex (SLC) images with HH polarization, acquired in 'High Resolution 5m Mode' (MDA, 2021) from different orbits during 2023–2024 (Table 1). This mode has a nominal resolution (i.e., theoretical resolution, which is based on radar system parameters) of 5 m and a swath width of 30 km. The native SLC pixel spacing is 1.4–2.8 m in the range direction and 2.4–2.8 m in the azimuth direction depending on the incidence angle (Table 1). The RCM SAR images were employed 1) to compute changes in the Milne Glacier surface, which allowed for flexure zone and hinge line delineation and quantification of floating ice tongue vertical displacement, and 2) to estimate ice velocities to compare with GNSS observations discussed in Section 2.2.3.

Table 1. Description of RCM datasets acquired between February of 2023 and September of 2024 for Milne Glacier flexure-zone (FZ) delineation and velocity estimates described in Section 2.2.3.

Relative orbit ID and derived results: flexure zone (FZ) and/or velocity (V)	Orbit pass: Des./ Asc.	Incidence angle (degrees)	SAR parameters for error calculations (Eq. 2): Incidence angle,	Raw image pixel size Range (m) x azimuth (m)	Period of data acquisitions yyyy.mm.dd (time UTC ± 1 min)	Number of FZ delineations

			Track angle[1] (degrees)			
09 FZ, V	Des.	38.5-40.6 (Swath 12)	**39.5[2],** 230	2.4 × 2.6	2023.02.17 – 2024.03.23 (13:19)	42
43 FZ	Asc.	19.0-21.9 (Swath 1)	20.3, -58.9	1.4 × 2.4	2023.03.07 – 2024.03.17 (19:58)	27
53 V	Des.	52.7-54.1 (Swath 23)		2.8 × 2.8	2023.03.08 – 2024.03.26 (12:06)	–
58 FZ, V	Asc.	20.1-23.1 (Swath 2)	21.5, -58.0	1.4 × 2.4	2023.03.12 – 2024.03.26 (20:06)	25
73 V	Asc.	22.2-25.1 (Swath 3)		1.4 × 2.6	2023.03.13 – 2024.03.27 (20:13)	–
103 FZ	Asc.	26.3-28.9 (Swath 5)	27.5, -55.0	1.4 × 2.5	2023.03.11 – 2024.09.17 (20:30)	22

[1] Azimuth (clockwise from True North)

[2] The incidence angle of orbit 09 is 1.4 - 2 times greater than that of orbits 43, 58, and 103.

To delineate the flexure zone, the RCM images were processed using the DDInSAR method (Rignot, 1996). This method reveals the surface displacement of the floating ice tongue along the SAR line-of-sight, by removing the effect of steady glacier flow, by differencing two consecutive interferograms, under the assumption that the glacier velocity remains constant between SAR data acquisitions. The hinge line and the hydrostatic line are then manually or automatically delineated by examining the landward and seaward limits of the fringe pattern in the DDInSAR images representing the flexure zone. We used GAMMA (Werner et al., 2000) to compute the differences in the SAR phase and quantify changes in the surface height between data acquisitions. Interferograms were computed for each pair of RCM data acquisitions with a 4-day interval. During processing, we applied 3 × 3 multilooking to reduce speckle, improve the signal-to-noise ratio and interferometric coherence, and reduce file sizes to facilitate phase unwrapping. After multilooking, the effective ground pixel spacing was approximately 9–10 m. Topographic phase removal and terrain correction were performed using the 10 m ArcticDEM dataset (Porter et al., 2023). Interferograms were unwrapped using the minimum-cost flow phase unwrapping algorithm described by Costantini (1998). During the initial unwrappig, the processing software automatically selected an arbitrary stable reference area. Then, differential interferograms were calculated at 10 m resolution (i.e., the final spatial resolution of DDInSAR images used for flexure zone delineations) and the corresponding unwrapped results represented by three consecutive data acquisitions (over 8 days) or four data acquisitions (over ≥12 days) if there was a gap between data acquisitions. The final calibration of the SAR

line-of-sight displacement was conducted along three transects (Fig. 1, described below) using an automated script. Values were divided by the cosine of the incidence angle and additionally calibrated to the mean values of the grounded portions of the transects for each DDInSAR image from orbits 09 and 103. Phase jumps exceeding 2 cm (i.e., a more conservative threshold than half of the RCM C-band wavelength) were corrected for all orbits.

The western and eastern flexure-zone boundaries were often affected by noise. These areas of low interferometric coherence typically occur due to strong velocity gradients, shear, ice deformation, and rotation as glacier velocities decrease from the centre toward the lateral margins as a result of lateral drag (Forster et al., 1999; Mannerfelt et al., 2025). These processes contribute to ice weakening and reduced stiffness in lateral shear zones (e.g., a fivefold reduction in Young's modulus was reported by Wild et al., 2025). This interpretation is supported by our in situ observations and high-resolution imagery demonstrating extensive crevassing in this zone, particularly along the western margin of Milne Glacier, where a tributary glacier further enhances these processes. The resulting loss of coherence in the flexure-zone's western and eastern boundaries prevented their reliable delineation and the use of the entire area of the flexure zone for our analysis. Instead, changes to the flexure zone were quantified as follows. The flexure-zone boundaries were manually delineated using geographic information system (GIS) software and analysed along three transects on the western, central and eastern sides of the glacier, denoted by subscripts: W, C, E, respectively (Fig. 1). Each of these transects has known surface and bed topography (Fig. 1 a and Fig. 9 in the Results section) from airborne and in situ radar observations (CReSIS, 2021; Antropova et al., 2024). The transects start up-glacier at an arbitrary fixed point (A) at km 32 along the 2014 IceBridge radar transect. In a given DDInSAR image (denoted by numbered subscripts), the three transects cross the hinge line at point B and the hydrostatic line at point C. We used the following variables to characterize the temporal evolution of the flexure zone:

- flexure-zone width (e.g., for DDInSAR image 1, distance between B_{W1} and C_{W1} in Fig. 1);
- surface displacement in the vertical direction;
- distance to hinge line from the fixed point A (e.g., distances between A and $B_{W1,}$ A and $B_{C1,}$ and A and B_{E1} in Fig. 1);
- grounding-zone width (i.e., the distance along the glacier between the most landward and most seaward hinge-line delineations based on all DDInSAR images over the entire observation period). For illustrative purposes, the grounding zone is shown by the distance between B_{W1} and B_{W2} in Fig. 1, based on DDInSAR image 1 and 2 associated with data acquisitions in March-April 2024 and September 2024.

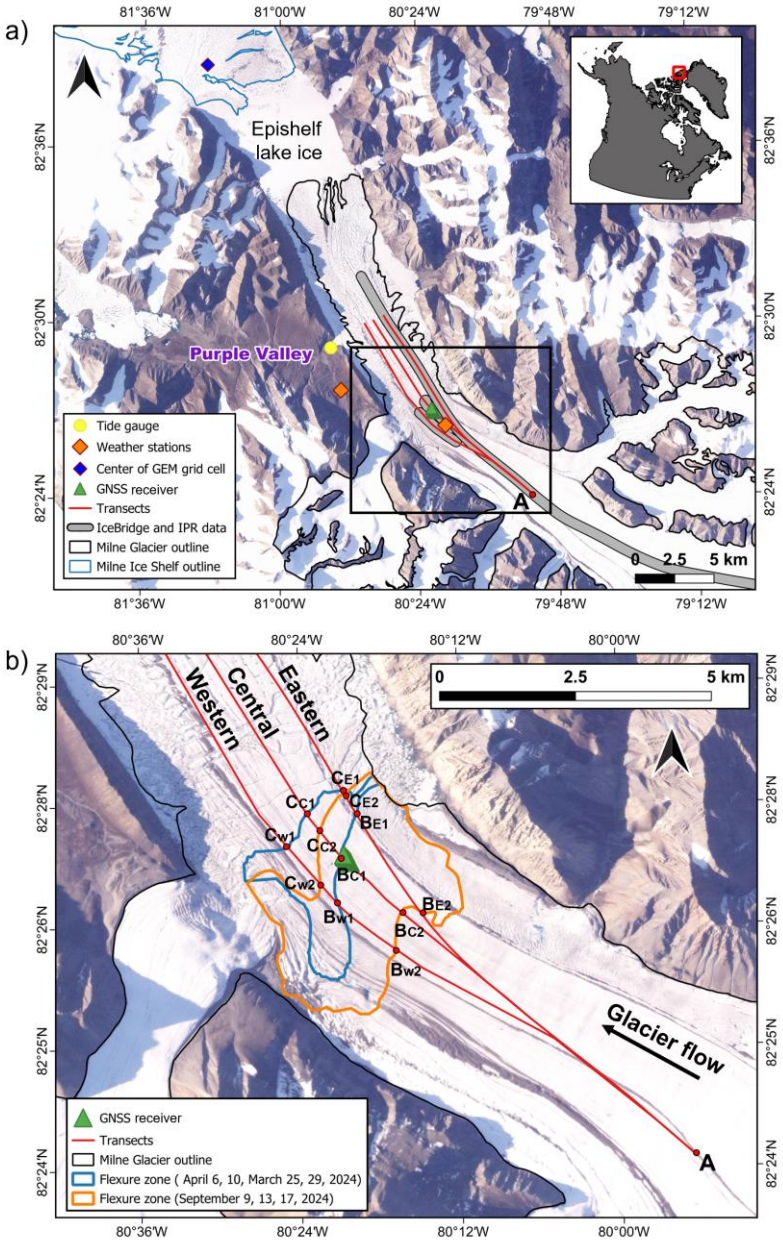


Figure 1: Study site. a) Locations of Milne Glacier, in situ instrumentation, and Global Environmental Multiscale (GEM) grid cell centre. b) Milne Glacier tidal-flexure zone with two examples of its delineation based on SAR images acquired (1) between March 25 and April 10, 2024 (blue polygon) and (2) September 9 and 17, 2024 (orange polygon) shown over a Planet image acquired on August 12, 2024 (Image © [2024] Planet Labs PBC). Flexure-zone variables explored in this study are computed along the western, central, and eastern transects (subscript W, C, and E) shown in red (through points A, B and C). These variables include: 1) distance to hinge lines (A to B_{W1}, A to B_{C1}, A to B_{E1} for flexure zone in DDInSAR image 1, blue polygon, and A to B_{W2}, A to B_{C2}, A to B_{E2} for flexure zone in DDInSAR image 2, orange polygon), 2) width of the two flexure zones (B_{W1} to C_{W1}, B_{C1} to C_{C1}, B_{E1} to C_{E1} and B_{W2} to C_{W2}, B_{C2} to C_{C2}, B_{E2} to C_{E2}), 3) Grounding-zone width (B_{W1} to B_{W2}, B_{C1} to B_{C2}, B_{E1} to B_{E2}), and 4) surface displacement height of the floating ice.

2.2.2 Analysis of tides and reconstruction of ice-surface height timeseries

The vertical component of DDInSAR-derived surface displacement of the floating part of the glacier was analysed with respect to the changes in sea surface height (SSH) due to tides and atmospheric pressure. We used tidal constituents derived from in situ tidal observations recorded every 6 seconds with an RBR Duet datalogger deployed at ~10 m depth in a lateral bay on the western side of Milne Fiord (i.e., tide gauge location in Fig. 1 a) between September 3, 2016 and July 4, 2017 to simulate tides at a 1-minute interval for the period of SAR observations using the T_TIDE toolbox (Pawlowicz et al., 2002). Simulated tide heights were corrected by adding the inverse barometer effect (IBE) (Wunsch & Stammer, 1997; Padman et al., 2003), while ocean tide loading on the Earth's crust was neglected, as it has a relatively minor impact (Wild et al., 2025). We used the atmospheric pressure data recorded every 30 minutes by our in situ weather stations (Fig. 2 c). Gaps in the in situ pressure records (i.e., July 9–21, 2023, with no associated DDInSAR images, and July 22–September 17, 2024, with one DDInSAR image) were filled using the Global Environmental Multiscale (GEM) model output (Buehner et al., 2015). The GEM model-based data at a 1-hour interval were extracted for a GEM grid cell of about 15 km × 15 km centred at 82.6477°N, 81.3225°W on the Milne Ice Shelf about 9 km to the northwest of the glacier terminus, to avoid the influence of higher elevations in grid cells closer to the grounding line (Fig. 1).

Both air temperature and surface pressure were in good agreement with in situ observations (Fig. 2). In particular, the correlation between the GEM model and in situ atmospheric pressure records used for IBE calculations was 0.96, with a root mean squared error (RMSE) of 3.6 hPa, and a bias of -2.4 hPa. To calculate the IBE over the entire observation period, we assumed that a 1 hPa change in atmospheric pressure results in a corresponding -1 cm change in sea level (Wunsch & Stammer, 1997; Padman et al., 2003). This correction was linearly interpolated to a 1-minute interval and then added to the simulated tides to compute the SSH. The SSH computed using T_TIDE showed a higher correlation (0.96 vs. 0.93) and lower RMSE (3.4 cm vs. 4.6 cm) than the independent tidal model GR1kmTM (Howard and Padman, 2021), when compared with repeated in situ tidal observations collected in July 2023 (Fig. A1). This supports the choice of the T_TIDE algorithm for our analysis. DSSH, the difference in SSH for each DDInSAR image, was calculated by subtracting the SSH values at the times of SAR data acquisition, consistent with the DDInSAR combinations. We assessed the relationship between DSSH and DDInSAR-derived surface height displacement of the freely-floating ice tongue (i.e., mean values calculated from 44 km downfjord along the three transects in Fig. 1) based on the correlation coefficient, the root mean squared error (RMSE), and bias.

To explore the origin of the newly developed notch along the eastern margin, we tested the hypothesis that it appears in DDInSAR images associated with SAR acquisitions during periods of high SSH, suggesting that seawater intrudes farther inland and results in ice ungrounding around a pinning point. We used the minimum and maximum SSH values, as well as the standard deviation, for each DDInSAR result associated with three or four SAR data acquisitions. These values were then divided into two groups corresponding to: (1) DDInSAR results without the notch and (2) DDInSAR results with the newly developed notch present, to test whether SSH differs significantly between the groups.

DDInSAR results provide information on differential ice-surface displacement; hence, reconstructing ice-surface height from DDInSAR observations at individual times could provide additional information. For example, a tide-deflection-ratio map (i.e., the ratio of tidal displacement at a given location to the displacement measured in a freely floating reference area derived from DDInSAR observations; Han and Lee, 2014) can be combined with a tide model to predict ice-surface displacement under individual tidal conditions across the SAR-covered area (Wild et al., 2019). Here, we employed a simplified approach without tide-deflection-ratio map to reconstruct the ice surface height timeseries by least square fitting of our DDInSAR displacements using 23 of the 59 tidal constituents with signal-to-noise ratios above 2 computed with the T_TIDE harmonic analysis (Pawlowicz et al., 2002) as well as IBE. We limited the reconstruction to DDInSAR-derived displacement of the freely floating ice tongue along the western and central transects and therefore did not take into account the ice response to changing tides within the flexure zone. The coefficients for each harmonic component were estimated using a regularized least-squares approach assuming a multifrequency harmonic function as follows:

$$d(t) = \sum_{j=1}^{N}\left[a_j \sin(\omega_j t) + b_j \cos(\omega_j t)\right] + cH(t) \quad (1)$$

where ω_j is the circular frequency corresponding to jth tidal constituent, $H(t)$ is the time-dependant IBE component, and a_j, b_j, and c are the least squares fitting coefficients (Appendix B), t is time of SAR data acquisitions. In (1) $j = 1$ corresponds to the most dominant tidal constituent and $j = N = 23$ corresponds to the least dominant tidal constituent. The decision to retain 23 out of the 59 constituents was based on their signal-to-noise ratio and their contribution to the decrease in RMSE (B1 b). The optimal regularization parameter ($\lambda = 3.6$) was determined using the L-curve analysis (Hansen, 1992) shown in Fig. B1 a.

2.2.3 Assessment of uncertainties in flexure-zone delineations due to velocity variability, ice bending, and SAR viewing geometry

To assess uncertainties in the flexure-zone delineations, we estimated the errors introduced into the computed SAR line-of-sight vertical surface displacement by velocity variability and by ice-surface extension and compression due to tidal bending. To investigate the effect of velocity variability on the grounding-line migration, we split our DDInSAR datasets from all orbits into two periods associated with steady and unsteady glacier velocity periods (Fig. 2 a) for the period of SAR data acquisitions. To define these two flow periods, we used in situ-measured and SAR-derived glacier velocities in the flexure zone supported by air temperature observations. In situ velocities along the central transect were obtained with GNSS receivers (Garbo, 2024) installed near the grounding line (Fig. 1) to record positional information between July 2022 and July 2024. The instruments recorded positional information for three hours daily (i.e., 16:00–19:00 UTC), yielding GNSS positions with an error of about 1.5 cm after static-mode precise point positioning processing (NRCan, 2024). The final GNSS position was represented by the mean latitude and longitude values stabilized between 18:00 and 19:00 UTC, which was close to the SAR acquisition times for orbits 43, 58, and 103, but involved a larger time gap for orbit 09. Thus, the GNSS measurements likely captured a more representative tidal signal for orbits 43, 58, and 103 than for orbit 09. The observed distances between the GNSS positions were converted to daily velocities (Fig. 2 a). The missing GNSS records (10.5% of the total records within the analysed periods)

at the end of the unsteady period and beginning of the steady period in 2024 were linearly interpolated from neighbouring observations and compared against SAR-derived velocity. The SAR-derived Milne Glacier velocity, averaged within a 3x3 pixel window at the GNSS receiver location (Fig. 1), is shown in Fig. 2a. To estimate the velocity, RCM SAR data acquired from four orbits (i.e., relative orbits: 09, 53, 58, and 73; Table 1) were employed to compute ascending and descending range and azimuth speckle offset products in GAMMA (Werner et al., 2000). Then, 3D displacement time series were derived from a set of linear equations using inverses (Samsonov et al., 2021). The interpolated values for the missing GNSS records agreed within ±0.01 m d^{-1} with SAR-derived velocities. These SAR-derived velocities demonstrated a surprising spike in January–February 2024 (Fig. 2 a). This spike coincided with a rise in air temperature and likely represented real glacier acceleration. However, because the GNSS receiver ran out of battery and did not record in situ measurements during this period, these records were excluded from the velocity variability analysis.

The steady and unsteady periods were defined based on the glacier velocity strictly within the period of DDInSAR data acquisitions to explore the effect of velocity variability on our DDInSAR-derived results and do not necessarily represent annual patterns in glacier dynamics. The steady period was defined as a period of invariant and low glacier velocity of about 0.4 m d^{-1} (SAR data acquisitions from February to May, 2023 and 2024, a period highlighted in blue in Fig. 2 a, b), which was predominantly associated with winter time and low air temperatures. Conversely, the unsteady period had changing velocity values that decreased from 0.6 m d^{-1} to 0.4 m d^{-1} (SAR data acquisitions from September to December 2023, a period highlighted in orange in Fig. 2 a, b), following a period of positive air temperatures and pronounced glacier acceleration in July and August (Fig. 2).

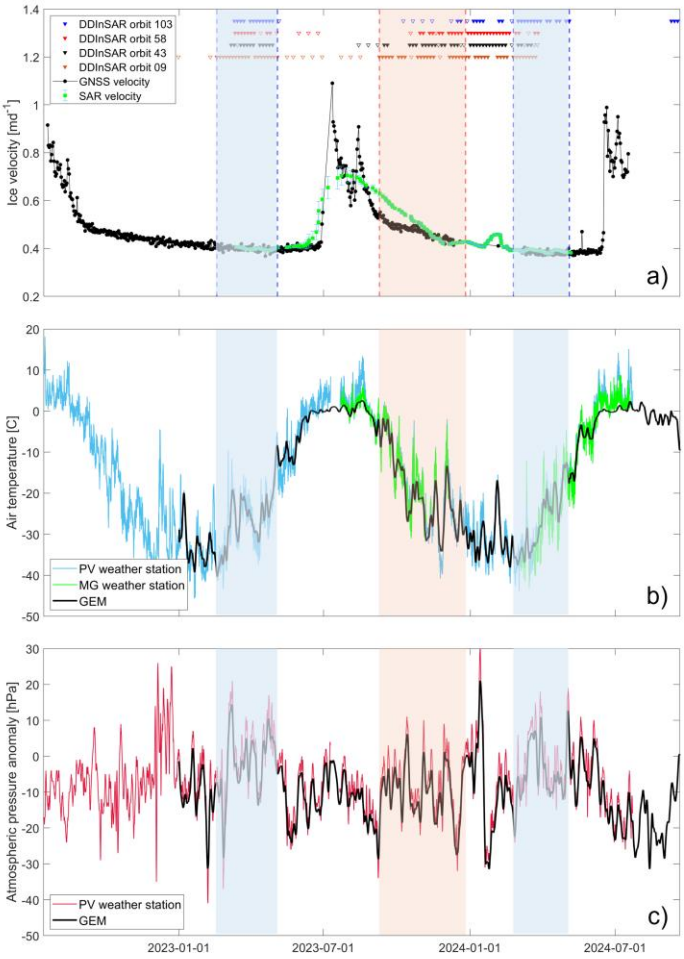


Figure 2: Milne Glacier ice velocity and meteorological observations. a) Daily ice velocity measured with GNSS receivers (black line) and calculated from SAR data (green line) in the flexure zone. b) Air temperature recorded on Milne Glacier (MG), in Purple Valley (PV), and retrieved from the GEM model. c) Atmospheric pressure anomaly (i.e., difference from 1013 hPa) recorded in Purple Valley, overlayed with GEM data, used to calculate SSH. The winter SAR observation block associated with a steady glacier period, highlighted in blue, corresponds to relatively steady and low velocity values of 0.4 m d^{-1}. The fall SAR observation block associated with an unsteady period, highlighted in orange, corresponds to velocity values decreasing from 0.6 m d^{-1} to 0.4 m d^{-1}. SAR data acquisition times for four different orbits are shown with triangles: filled if flexure zone delineation was made, or empty if not, due to low coherence.

The correlation between DSSH and DDInSAR-derived height was calculated for both the steady and unsteady periods and analysed with respect to glacier acceleration computed for the corresponding SAR data acquisition times. Acceleration was calculated as a local slope for five GNSS velocity records within a ±2-day time window centred on the day of each SAR data acquisition used in the DDInSAR processing.

The error introduced to the line-of-sight surface displacement due to varying ice velocity between SAR data acquisitions in the computed DDInSAR displacement, was assessed by calculating the absolute line-of-sight horizontal error, ε_{LOShV},:

$$\varepsilon_{LOShV} = |\Delta D \times cos\gamma| \quad (2),$$

where ΔD is the GNSS-derived difference in glacier displacement between the first and the second SAR image pairs used for the DDInSAR computations, γ is the angle between the 3D-vectors of glacier velocity (taking into account the mean glacier flow heading of 317.7° with respect to True North and the mean glacier surface tilt of 3.5° in the flexure zone) and SAR line-of-sight for each orbit (taking into account the incidence and track angles shown in Table 1) calculated based on Eq. 1 in Samsonov (2024).

To assess the SAR line-of-sight error resulting from ice extension or compression due to tidal bending, we applied the elastic model described by Rack et al. (2017), using the minimum and maximum mean ice thicknesses of the grounding zone along the central and western transects (i.e., 200.5 m and 225.6 m, respectively). This analysis was limited to the available airborne and ground-based ice penetrating radar ice-thickness data along the transects (Fig.1). We assumed an elastic Young's modulus of 1.5 GPa, which is consistent with Rack et al. (2017) and is close to values reported for other glacier flexure zones (Wild et al., 2017, 2025). The maximum horizontal ice-surface deformation due to extension or compression (at a distance of 640.5 m and 699.5 m from the grounding line along the central and western transects, respectively) was modeled based on SSH at the times of SAR data acquisition. We chose to use SSH because it was more natural for the logic and sequence of our analysis, although we acknowledge that DSSH could also be used directly instead. We then calculated the differential horizontal ice-surface deformation due to bending, consistently with the DDInSAR image differencing. The absolute line-of-sight error due to bending, ε_{LOShB}, was calculated as follows:

$$\varepsilon_{LOShB} = |\Delta B \times cos\beta| \quad (3),$$

where ΔB is the horizontal ice surface deformation due to ice extension or compression and, β is the angle between the 3D-vectors of glacier tangent line and SAR line-of-sight for a corresponding orbit. Our modeled maximum slope angle of the glacier tangent line with respect to the neutral position (for a maximum SSH of ±0.5 m) was 0.02º; therefore, we assumed that $\beta \approx \gamma$.

The uncertainty of the delineated hinge-line positions was assessed based on the sum of the computed line-of-sight errors arising from variations in ice velocity and ice bending. This combined error was expressed as a fraction of a SAR fringe, representing a vertical displacement of half the wavelength (i.e., 2.75 cm for RCM). To estimate the horizontal extent corresponding to a fraction of a SAR fringe, the typical fringe width along the central transect was calculated from the DDInSAR images used for flexure-zone delineation. A Laplacian filter was applied to the DDInSAR images to enhance fringe edges, after which fringe widths were computed for all images and the mean, median, and mode values were determined. Horizontal uncertainties were then calculated as fractions of the typical fringe width along the transect, represented by the median value.

2.2.4 Analysis of grounding-line migration and grounding-zone width

Flexure-zone variables such as distance from point A (Fig. 1) to the hinge line and the flexure-zone width along the three transects (Fig. 1) were examined with respect to glacier geometry and SAR-derived velocities over period of observations. In particular, bed and surface slopes retrieved from the airborne IceBridge radar data recorded in 2014 and ground-based ice penetrating radar (IPR) transects collected between 2016 and 2023 (Fig. 1, details described in Antropova et al., 2024) were employed. The surface elevation derived from the airborne and ground-based radar datasets was also compared against ArcticDEM (Porter et al., 2023), a digital elevation product based on optical stereo imagery collected between 2008 and 2021 over Milne Glacier. The distance from point A to the hinge line (B) was calculated for all orbits to investigate patterns of landward and seaward grounding-line migration. The Milne Glacier grounding-zone width for the entire period of observations (2023 - 2024) was calculated as the difference between the maximum and minimum distances from point A to the most seaward and landward DDInSAR-derived hinge lines, respectively, along the three transects (e.g., max |A B_W| – min |A B_W| for the western transect). These results were compared with grounding-zone width derived from DDInSAR images from orbits 43 and 103 within the steady period, which are associated with the lowest line-of-sight errors due to velocity variability and tidal bending and are therefore considered the most reliable.

In addition, we assessed the theoretical width of the grounding zone (ΔL) for the three transects shown in Fig. 1 with the known surface and bed geometry based on the following equation (Tsai & Gudmundsson, 2015):

$$\Delta L = \Delta h_{high}\left((\alpha-\beta)\frac{\rho_i}{\rho_w}+\beta\right)^{-1} + \Delta h_{low}\left(\frac{\alpha\rho_i}{\rho_w\left(1-\frac{\rho_i}{\rho_w}\right)}+\beta\right)^{-1} \quad (4),$$

Where Δh_{high} and Δh_{low} are the highest (0.50 m) and lowest (-0.44 m) SSH during the period of observations, α and β are surface and bed slopes calculated over the entire distance of available in situ IPR observations and from 38 km to 42 km of the IceBridge transect (Fig. 9), ρ_i and ρ_w are ice (917 kg/m^3) and water densities (1025.4 kg/m^3, an average value for 100-200 m depth in Milne Fiord), respectively. This equation was derived by Tsai and Gudmundsson (2015) based on prograde bed geometry and was later applied to both retrograde and prograde bed geometries (e.g., Chen et al., 2023), assuming negligible bending stresses at the ice surface. The calculated theoretical width of the grounding zone was compared against the SAR-derived one. Finally, IPR-derived bed topography and SAR-derived velocity in the grounding zone were used to interpret processes of ice dynamics and deterioration in this critical zone.

3. Results

3.1 DDInSAR results

We delineated 116 flexure zones, from four different orbits (Fig. 3) using the DDInSAR technique applied to three RCM SAR scenes when there were no gaps in the 4-day acquisition cycle, or to four RCM SAR scenes when gaps occurred. Our

delineations revealed short-term fluctuations and systematic changes in the flexure zones, with the flexure zone's width along-glacier flow varying from 46 m to ~2.9 km (Table 2). The resulting minimal flexure-zone widths were consistent among the four orbits: with the smallest values along the eastern transect, followed by the values for the central transect, and the largest values along the western transect. The ice thicknesses at the most landward hinge line did not vary substantially (255–263 m). Maximum flexure-zone width values were consistently higher for the western transect, but values for the eastern transect were often larger than for the central transect.

Table 2. Milne Glacier flexure zone widths over the period of observations. Ice thicknesses are shown for the most landward hinge-line positions for each transect.

Relative orbit ID	Western transect (ice thickness: 263 m), min – max (m)	Central transect (ice thickness: 260 m), min – max (m)	Eastern transect (ice thickness: 255 m), min – max (m)
09	641 – 2873	485 – 2222	46 – 2422
43	862 – 2760	548 – 2223	188 – 2153
58	888 – 2896	620 – 2395	358 – 2522
103	770 – 2744	561 – 2125	323 – 2574

Hinge lines derived from DDInSAR images between February and September 2023 were asymmetric with a pronounced notch at the glacier's western margin, as reported by Antropova et al. (2024; Fig. 3). However, several interferograms between October 2023 and September 2024 exhibited a new notch in the flexure zone at the glacier's eastern margin. As a consequence, the glacier flexure zone's eastern edge, that had a much lower average grounding-line retreat rate (29 m yr^{-1}) than its central (53 m yr^{-1}) and western (124 m yr^{-1}) regions between 2011 and 2023 (Antropova et al., 2024), experienced rapid changes toward the end of the current observation period. The grounding-line retreat on the eastern side occurred around a pinning point associated with a "bull's-eye" pattern in the DDInSAR interferograms (Fig. 3 d and Fig. A2), similar to the bull's-eye pattern near the western side of the glacier observed by Antropova et al. (2024). The grounding line shifted up-glacier by 1 km compared to the most landward position observed during March 27-April 4 2023 in our previous study (i.e., Antropova et al., 2024), and exhibited a shift of approximately 690 m along the eastern transect between the most landward hinge-line positions derived from all DDInSAR images with and without the notch in this study. This shift was even more pronounced farther east, where the notch advanced landward by 2.5 km compared to the last reported position and by 2.4 km (measured parallel to the eastern profile) for observations with and without the notch during the period covered by this study.

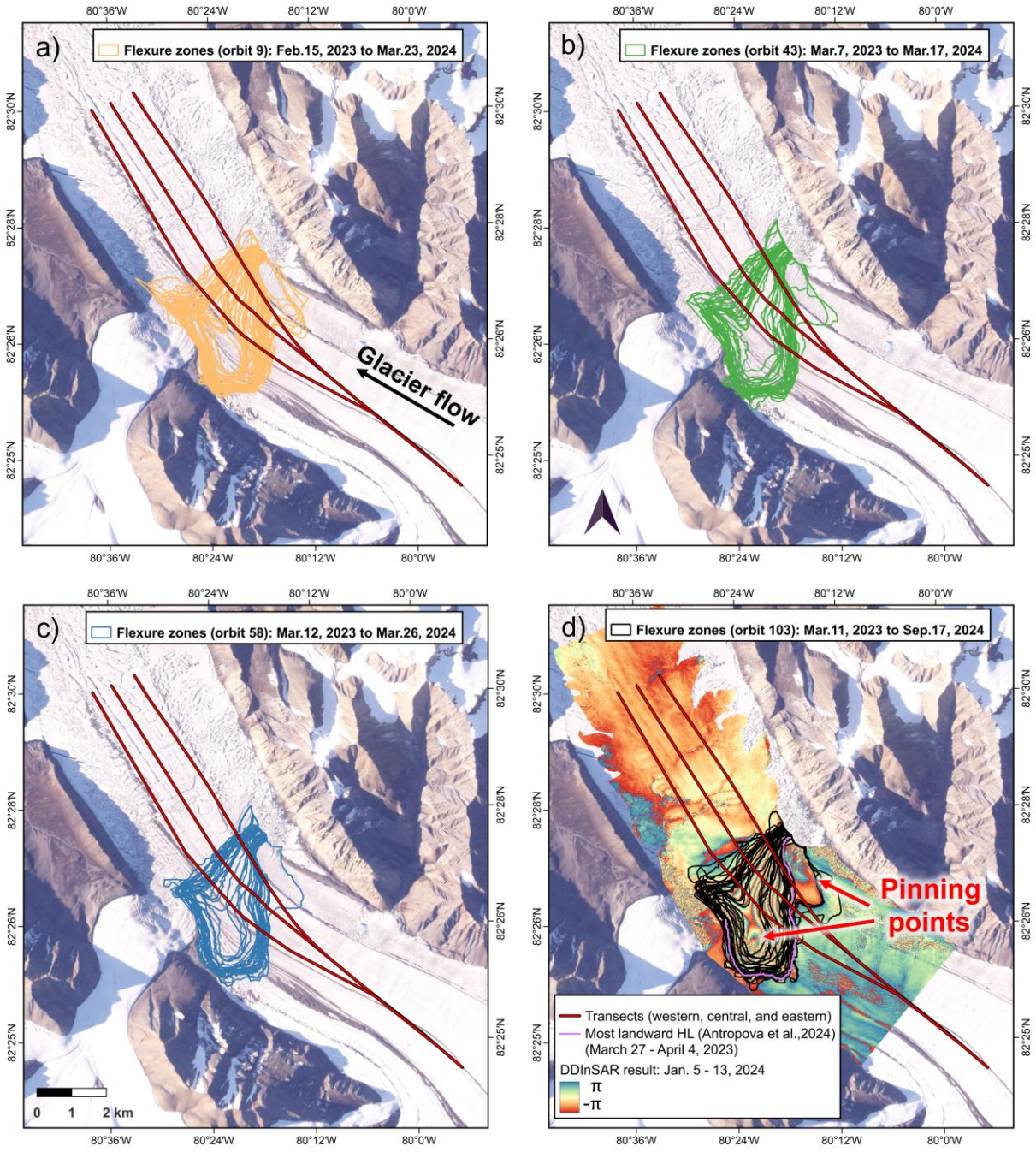


Figure 3: Flexure-zone delineations based on 2023-2024 RCM data acquisitions and overlayed on a Planet image acquired on August 12, 2024 (Image © [2024] Planet Labs PBC). a) Orbit 09 delineations: 42 orange polygons. b) Orbit 43 delineations: 27 green polygons. c) Orbit 58: 25 blue polygons. d) Orbit 103: 22 black polygons overlying a DDInSAR example showing pinning points on both sides of the glacier. A pronounced retreat associated with the formation of a new notch around the pinning point (Fig. A2) at the eastern margin was discovered in October 2023, after the March-April 2023 hinge line delineations by Antropova et al. (2024).

3.2 Tidal analysis and ice-surface height reconstruction results

In Milne Fiord, the T_TIDE-simulated tidal range spanned from –20 cm to 21 cm over the observation period. After adding IBE, the range increased 2.3-fold, spanning from –44 cm to 50 cm. T_TIDE-simulated tides that were IBE-corrected with in situ atmospheric pressure (i.e., differential displacement of sea surface height, DSSH) had a higher correlation with DDInSAR-derived displacement of the freely-floating ice surface (Fig. 4) than uncorrected simulated tides (Fig. A3 a-c) or simulated tides with GEM-based IBE-correction (Fig. A3 d-f). The western and central transects showed correlation coefficients (r) between DDInSAR-derived displacement and DSSH ranging from 0.81 to 0.94, RMSE values of 10.8 to 15.7 cm, and biases of -0.8 to 2 cm. The eastern side was not as well correlated (correlation coefficients ranging from 0.45 to 0.70, RMSE values of 20.0 to 24.6 cm, and biases of -0.2 to 2.9 cm), as it was mostly grounded throughout the study period, yielding very small DDInSAR-derived surface displacements.

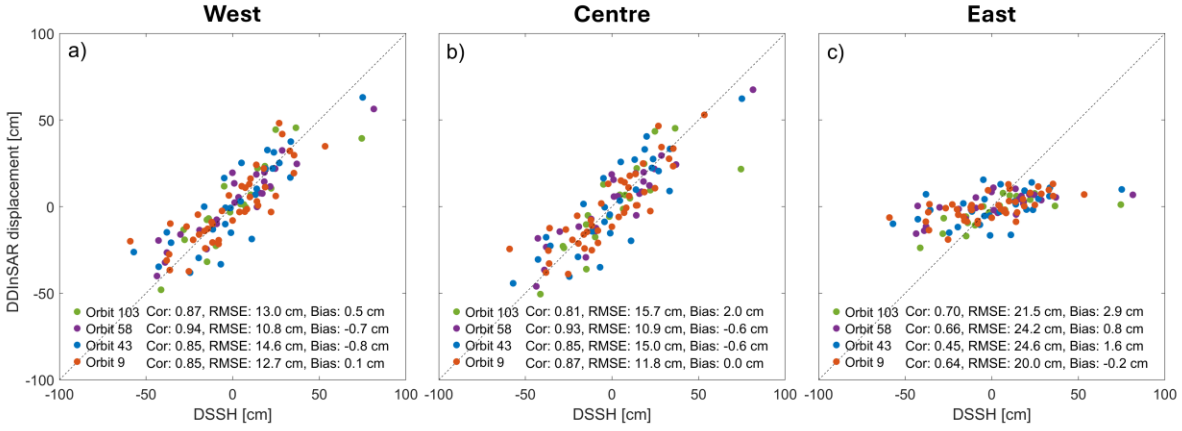


Figure 4: Relationships between DDInSAR displacement and differential displacement of sea surface height (DSSH) for the: q) western, b) central, and c) eastern transects. The different orbits are denoted by coloured symbols. 'Cor' - the Pearson correlation coefficient, 'RMSE' - Root mean square error, the 1:1 is plotted as a dashed line.

Surface displacement of the floating ice tongue, calculated from unwrapped DDInSAR imagery corrected for phase jumps, varied between -40 cm and 60 cm along both western and central transects (Fig. 5 a, b), but this variation was smaller (between -20 cm and 20 cm) along the eastern transect (Fig. 5 c). This also implies that, most of the time, the eastern part of the glacier, with ice thickness similar to the values measured along the central and western transects (Table 2), was grounded with negligible DDInSAR displacement. The shape of the surface displacement curves suggests that ice ungrounding mostly occurs between 38 and 40 km down-glacier from point A.

Two prominent surface displacement bumps, approximately 3 cm in height, located between 32 and 35 km, were derived from DDInSAR images based on SAR acquisitions with relatively large temporal gaps. Specifically, the first DDInSAR image was generated from RCM data acquired on September 15 (SSH: −8.3 cm), September 19 (SSH: −7.9 cm), October 17 (SSH: 4.4

cm), and October 21 (SSH: 9.8 cm) 2023. The second DDInSAR image was computed from acquisitions on October 21 (SSH: 9.8 cm), October 25 (SSH: 13.8 cm), November 2 (SSH: −8.6 cm), and November 6 (SSH: 6.3 cm) 2023. Our uncertainty analysis results, discussed in detail below and shown in Fig. 7, confirmed that the absolute errors due to ice bending were relatively low (0.02 cm and 0.04 cm for the first and the second DDInSAR images, respectively) and smaller than the overall mean error of 0.06 cm. In contrast, velocity variability-related errors (i.e., 0.57 cm and 0.39 cm for the first and the second DDInSAR images, respectively) exceeded the unsteady-period mean value of 0.24 cm. Therefore, we attribute these bumps to velocity variability and the associated surface changes occurring within the acquisition intervals.

Both of these curves also illustrate an additional noticeable displacement trend of diverging from zero at approximately 36 km and subsequently increasing or decreasing up to 7 cm at 41 km, which could be explained by the combined effect of ice bending and velocity variability. The same trend was observed in two other DDInSAR images based on SAR acquisitions from: 1) November 6, 2023 (SSH: 6.4 cm), November 10, 2023 (SSH: 4.9 cm), and November 14, 2023 (SSH: −0.8 cm); and 2) February 10, 2024 (SSH: −3.3 cm), and February 14, 2024 (SSH: −12.1 cm), March 1, 2024 (SSH: 4.5 cm), March 5, 2024 (SSH: 19.4 cm). Absolute errors due to velocity variability were similar to or smaller than the steady-period mean of 0.06 cm (i.e., 0.06 cm and 0 cm for the first and the second DDInSAR images, respectively), whereas absolute errors due to ice bending (0.15 cm and 0.08 cm for the first and the second DDInSAR images, respectively) exceeded the mean error value of 0.06 cm. We therefore attribute these displacement patterns predominantly to the effect of bending. The pattern of curve deflection from zero near the grounding zone due to ice bending and/or velocity variability was even more pronounced in the DDInSAR displacement results from Orbit 09 and negligible in the DDInSAR displacement results from Orbit 103 (Fig. A4).

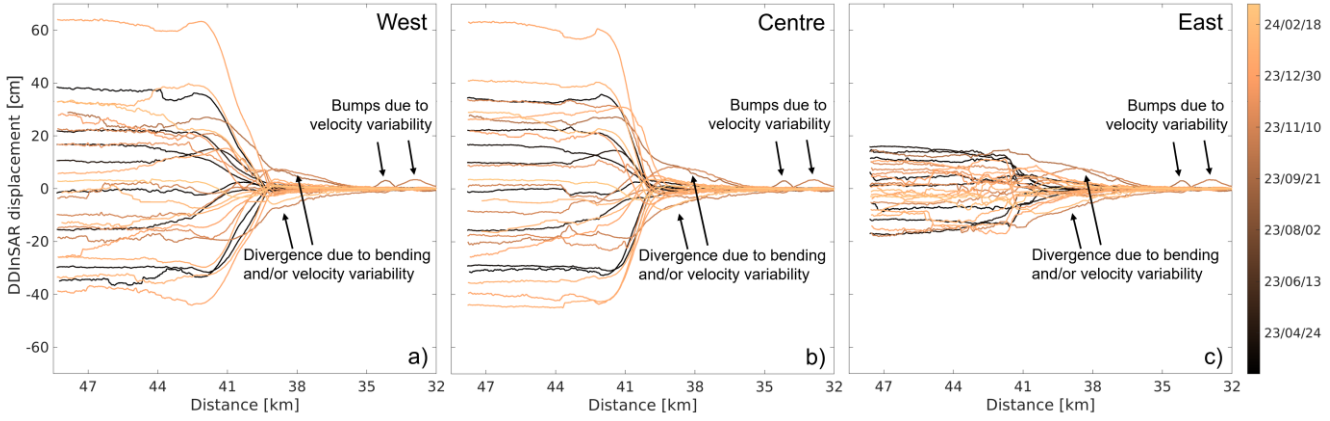


Figure 5: An example of DDInSAR-derived surface displacement from orbit 43 along the: a) western, b) central, and c) eastern transects starting at km 32 of the 2014 IceBridge radar profile (i.e., point A in Fig. 1). The line-of-sight errors due to tidal bending and velocity variability for orbit 43 are relatively low (Fig. 7 c, d). During the steady period, the combined line-of-sight mean error is 0.12 cm, whereas during the unsteady period it is 0.3 cm. These errors result in uncertainties of ±7.4 m (i.e., less than one pixel) and ±18.4 m (i.e., less than two pixels), respectively, for the hinge-line delineations.

Our hypothesis that the newly observed notch formed during periods of high SSH, leading to seawater intrusion and ice ungrounding around the eastern pinning point, was evaluated using statistical characteristics of SSH (i.e., sea surface heights at the time of SAR data acquisitions rather than their displacement values of DSSH) along the eastern transect. The calculated characteristics for the DDInSAR results were divided into two groups 1) cases without the notch, and 2) cases when the notch was observed (Table 3). Average minimum SSH conditions were similar (-0.09 m vs. -0.08 m) for both groups of our results, which was also confirmed by the two-sample t-test with high p-value of 0.8. The average maximum SSH was higher for observations associated with the notch presence (0.21 m vs. 0.13 m for observations with and without a notch, respectively). A two-sample t-test resulted in a low p-value of 0.009, confirming the statistical significance of this difference. The standard deviation was also higher for observations with the notch, than without (0.13 m vs. 0.10 m) since this group was associated with higher maximum SSH values. These results support the interpretation that higher SSH allows seawater to intrude farther inland, leading to the observed notch. The associated ice displacement and localized flexure around the eastern pinning point creates the characteristic "bull's-eye" pattern in our DDInSAR images.

Table 3. SSH statistical characteristics for the eastern transect.

Values averaged across all DDInSAR observations	Notch observed	No notch observed
Standard deviation (m)	0.13	0.10
Minimum SSH (m)	-0.09	-0.08
Maximum SSH (m)	0.21	0.13

The ice-surface height time series, reconstructed using a regularized least-squares approach based on 23 tidal constituents and DDInSAR displacements, is shown in Fig. 6 a. The demonstrated results are standalone and do not inform other analyses in this manuscript. The differential reconstructed ice surface displacement and DDInSAR displacement are highly correlated (r= 0.93) and yield an RMSE of approximately 8 cm for both the western and central transects during the steady period, which is reasonable given that our SSH showed a correlation of 0.96 and an RMSE of 3.4 cm with in situ tidal observations (Fig. A1). Future acquisition of independent GNSS observations over the freely floating glacier at tidal timescales could provide further opportunities to reliably assess our reconstruction results and associated uncertainties.

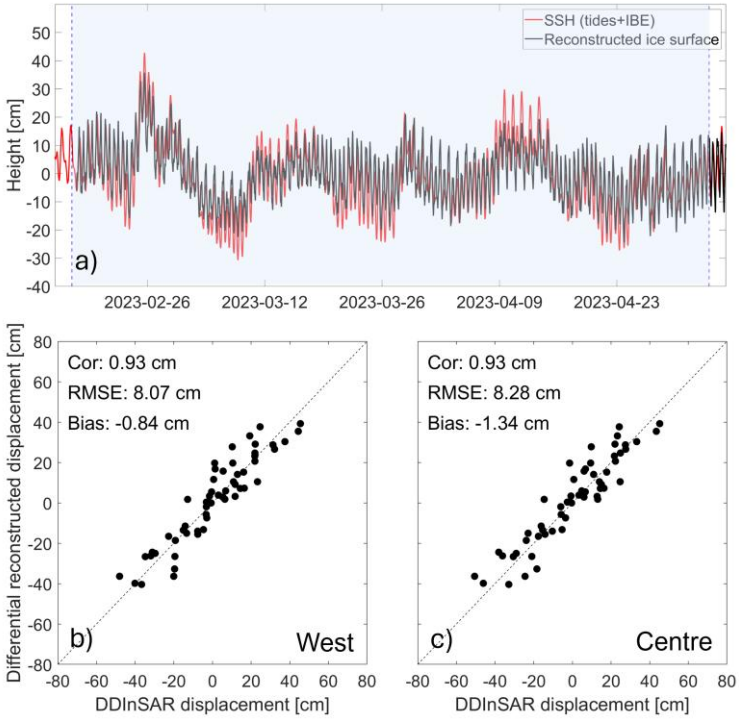


Figure 6: Reconstructed ice surface height. a) Time-series of ice surface heights and sea surface heights (SSH, i.e., tides and the inverse barometer effect, IBE) during the steady period, highlighted in blue. Relationship between the differential reconstructed ice surface displacement and DDInSAR-based displacement calculated along the: b) western and c) central transects. Number of observations is 55.

3.3 Uncertainty analysis results

Our results indicate differences between steady and unsteady glacier velocity periods along both the western and central transects in all four orbits (Fig. A5). The steady period has lower mean deceleration (0.02 cm/d^2 vs. 0.12 cm/d^2) and higher DSSH vs DDInSAR-derived displacement correlation (0.87 vs. 0.82) relative to the unsteady period. The resulting error due to velocity variability (LOShV) is threefold higher during the unsteady period than during the steady period (1.23 cm vs. 0.4 cm). Moreover, the error due to ice bending (LOShB) is also higher during the unsteady period relative to the steady period (0.52 cm vs. 0.37 cm along the central transect and 0.54 cm vs. 0.38 cm along the western transect).

These results are more informative when examined with respect to each of the four orbits, as the sensitivity of DDInSAR measurements to vertical and horizontal motion components depends on the incidence angle and look geometry (e.g., Rocca et al., 2010; Hu et al., 2014, Rack et al., 2017, Wild et al., 2018). The correlation between DSSH and DDInSAR-derived displacement, mean LOShV error and mean LOShB error for steady and unsteady periods in each of the four orbits are shown in Fig. 7. We again found that mean absolute deceleration and mean LOShV error values were consistently lower for the steady

period than for the unsteady one for all four orbits. The mean LOShB errors were low (0.05 cm – 0.10 cm) for ascending orbits with low incidence angles (i.e., orbits 43, 58, and 103) but were relatively high (0.86 cm – 1.02 cm) for the descending orbit with high incidence angle (i.e., orbit 09) during both periods.

The ascending orbits with low incidence angles showed high correlation between DSSH and DDInSAR displacement (0.91 – 0.95 in Fig.7 c, e, g) for the steady period, which was higher than correlation shown for the unsteady period (0.54 – 0.80 in Fig. 7 d, f). RCM orbit 43 results were associated with 11 times higher deceleration during the unsteady than the steady period (-0.11 cm/d^2 vs. 0.01 cm/d^2), which resulted in a 4-fold increase in LOShV error (0.06 cm vs. 0.24 cm) and the lowest observed correlation (0.54) between DSSH and DDInSAR displacement. This example underscores that pronounced changes in velocity violate the DDInSAR assumption of invariant velocities between SAR data acquisitions and reduce the correlation between DSSH and DDInSAR displacement. Therefore, the DDInSAR images should be interpreted with consideration of errors arising from variable velocity. Descending orbit 09, with a high incidence angle, exhibited the opposite pattern: a higher correlation during the unsteady period than during the steady period (0.93 vs. 0.83 in Fig.7 a, b), which we attribute to its higher sensitivity to horizontal displacement and, consequently to velocity variability as well as ice extension and compression due to tidal bending. The largest mean LOShB error (0.99 cm) for orbit 09 resulted from its more frequent high-tide observations compared to the other orbits during the unsteady period.

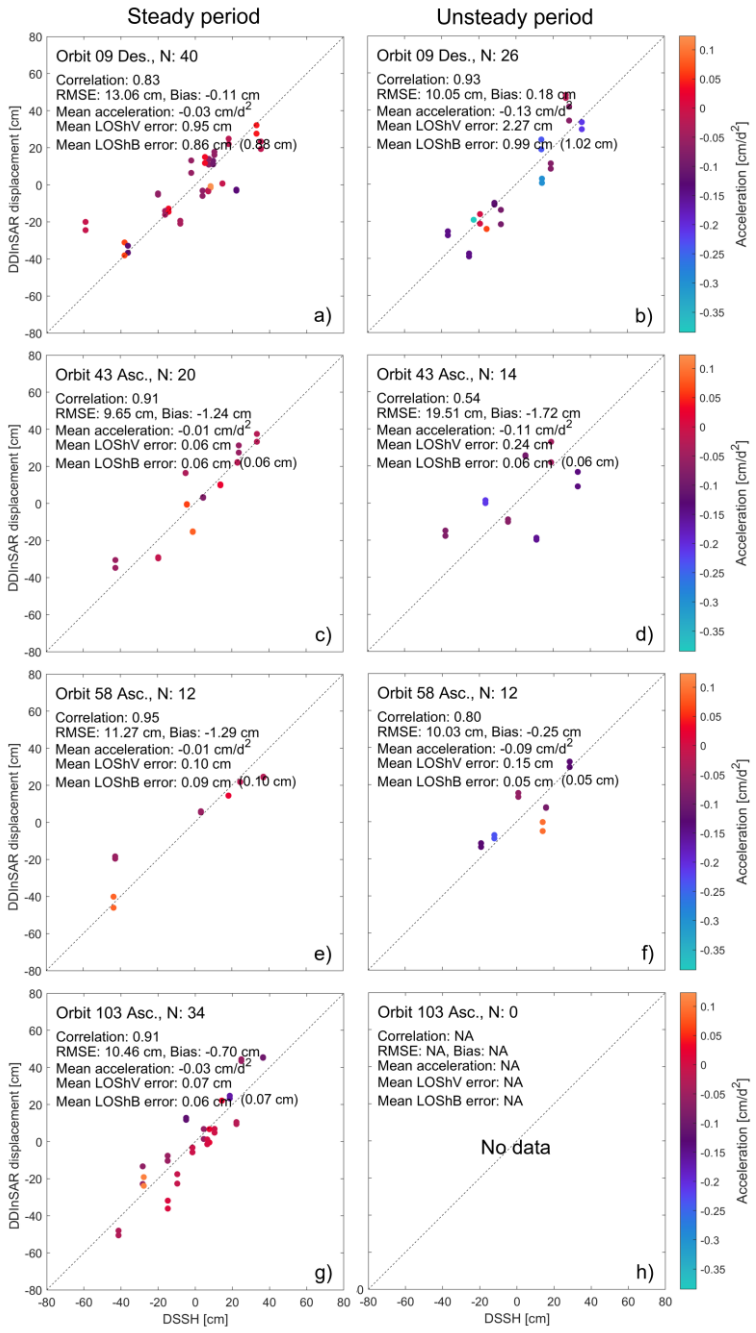


Figure 7: DDInSAR-derived vertical displacement versus differential displacement of sea surface height (DSSH) along the western and central transects with respect to the glacier velocity periods as defined in Fig. 2. Steady period with minimal changes in velocities and low line-of-sight errors for four orbits: a), c), e), g); and unsteady period with more pronounced changes in velocities and high line-of-sight errors for four orbits: b), d), f), h). LOShV represents error due to variable velocity based on in situ GNSS records, and LOShB represents error due to ice surface extension or compression from tidal bending along the central (western) transect.

The three ascending orbits with low incidence angles yielded the most reliable results, characterized by high correlations between DSSH and DDInSAR-derived displacements and the lowest mean LOShV and LOShB errors during the steady period. In contrast, descending orbit 09, acquired at a high incidence angle, exhibited the highest mean LOShV and LOShB errors during the unsteady period. Along the central transect during the steady period, the combined mean LOShV and LOShB errors for orbits 43 and 103 were 0.12 cm and 0.13 cm, respectively. These combined line-of-sight errors represented 4.4% and 4.7% of the vertical displacement detected within a single RCM DDInSAR fringe for orbits 43 and 103, respectively. Given the calculated median horizontal fringe width of 168.7 m (mean: 236.5 m; modal bin range: 100–120 m, representing 15% of total observations), the corresponding horizontal uncertainty during the steady period was approximately ±7–8 m, which is less than one pixel.

During the unsteady period for orbit 09, the maximum combined line-of-sight error along the central transect was 3.26 cm. Given the median horizontal fringe width of 187.1 m (mean: 212.5 m; modal bin range: 160–180 m, representing 16% of total observations), this corresponds to a horizontal uncertainty of ±221.8 m (i.e., approximately 22 pixels) for the flexure-zone delineations. Thus, flexure-zone delineations from orbits 43 and 103 during the steady period represent the most reliable results, with the lowest uncertainty, whereas delineations from orbit 09 during the unsteady period exhibit the greatest uncertainty.

3.4 Grounding-line migration and grounding-zone width results

The maximum and minimum distances from point A to the hinge line derived from all orbits are shown in Table 4, and the associated RCM SAR data acquisitions and SSH are presented in Fig. 8. The resulting grounding zone widths derived from these distances are generally larger for the western and eastern transects than for the central transect for all orbits, except for orbit 43. The largest grounding zone widths along the three transects are associated with orbit 103, which has low uncertainty (±8 m) during the stable period. In most cases (7 out of 12, highlighted in bold in Table 4), the standard deviation of SSH at the times of SAR acquisitions is higher for the minimum distance to the hinge line (i.e., the most landward hinge line position) than for the maximum distance (i.e., the most seaward hinge line position). Thus, the most landward hinge line positions are more often associated with larger SSH differences at the times of SAR acquisitions (Fig. 8).

Table 4. Results for the distances from point A to the hinge line, grounding-zone widths, and the associated SSH standard deviations.

Variables along the three transects	Relative orbit ID			
	09	**43**	**58**	**103**
Western transect:				
Distance: min – max (m)	6553 – 8414	6532 – 7352	6722 – 8208	6447 – 9048
Grounding zone width (m)	1861	820	1486	2601
SSH Standard deviation (cm) for min – max distances	**12.5 - 9.6**	10.3 - 13.4	9.7 - 9.8	8.5 - 10.1
Central transect:				

Distance: min – max (m)	7010 – 8379	7054 – 8256	7068 – 8364	6925 – 8850
Grounding zone width (m)	1369	1202	1296	1926
SSH Standard deviation (cm) for min – max distances	**13.2 - 9.6**	**10.3 - 7.3**	**29.8 - 9.8**	7.6 - 10.1
Eastern transect:				
Distance: min – max (m)	6786 – 8799	6999 – 8710	6880 – 8752	6684 – 8969
Grounding zone width (m)	2013	1710	1872	2285
SSH Standard deviation (cm) for min – max distances	**10.5 - 9.6**	**33.3 - 7.3**	**29.8 - 9.8**	7.6 - 10.1

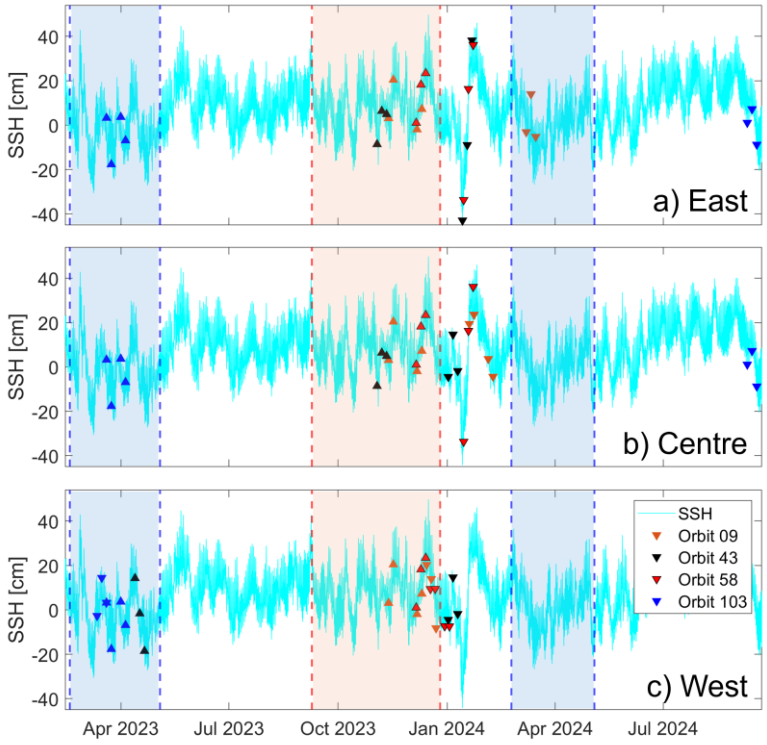


Figure 8: Timing of RCM SAR data acquisitions and the associated SSH values when the maximum (upward-pointing triangles) and minimum (downward-pointing triangles) distances from point A to the hinge line were detected in the DDInSAR images resulting from these acquisitions along the (a) eastern, (b) central, and (c) western transects. The steady velocity period is highlighted in blue, and the unsteady period is highlighted in orange.

Grounding zones derived from flexure-zone delineations during the steady period from orbits 43 and 103, which are characterized by the lowest uncertainty, as well as those for the entire study period, are shown in Fig. 9 a. The steady period grounding-zone width fully coincided with that of the entire study period for the western transect, and is smaller by 270 m and 306 m for central and eastern transects, respectively. The most landward grounding-zone limits for the entire study period along the central and eastern transects were based on orbit 103 RCM data acquisitions in September 9-17, 2024. Since this orbit is less sensitive to errors due to velocity variability and ice bending, this landward migration of the hinge line is likely

due to post-summer melt changes rather than uncertainty; thus, we consider the grounding zone width over the entire study period to be reliable. Therefore, the curve deflection from zero observed upstream of the grounding zone for Orbit 09 did not affect the final grounding-zone delineation (Fig. A4). The Milne Glacier grounding zone is associated with retrograde bed slopes along the three transects. The grounding-zone width over the entire study period was 2.3 km along the eastern, 1.9 km along the central and 2.6 km along the western transects (Fig. 9), which was about 55, 22 and 74 times larger, respectively, than calculated from the hydrostatic equation (Eq. 4). The western transect (Fig. 9 d), associated with the shallowest bed slope, had the largest grounding-zone width, whereas the central transect (Fig. 9 c), associated with the steepest slope, had the smallest grounding-zone width, which aligns with theory (Tsai & Gudmundsson, 2015) and observations from elsewhere (e.g., Rignot et al., 2024). In addition, our DDInSAR images suggest the presence of a pinning point farther westward of the bed rise ('BR3' in Fig. 9 d) between km 38 and km 39 of the western transect. This likely further amplifies the effect of the shallow slope by bridging the ice to the area where the bathymetry becomes shallower up-glacier of the tributary glacier that merges with Milne Glacier. The eastern bed slope was also associated with the pinning point shown by our DDInSAR images, which extended between the two bed rises at km 39.7 and km 40.7 highlighted in grey in Fig. 9 b. This pinning point altered the bed slope and the width of the observed grounding zone as it was linked to a pronounced retreat of the grounding line over the last portion of our SAR observation period, caused by seawater entering a cavity up-glacier of the pinning point.

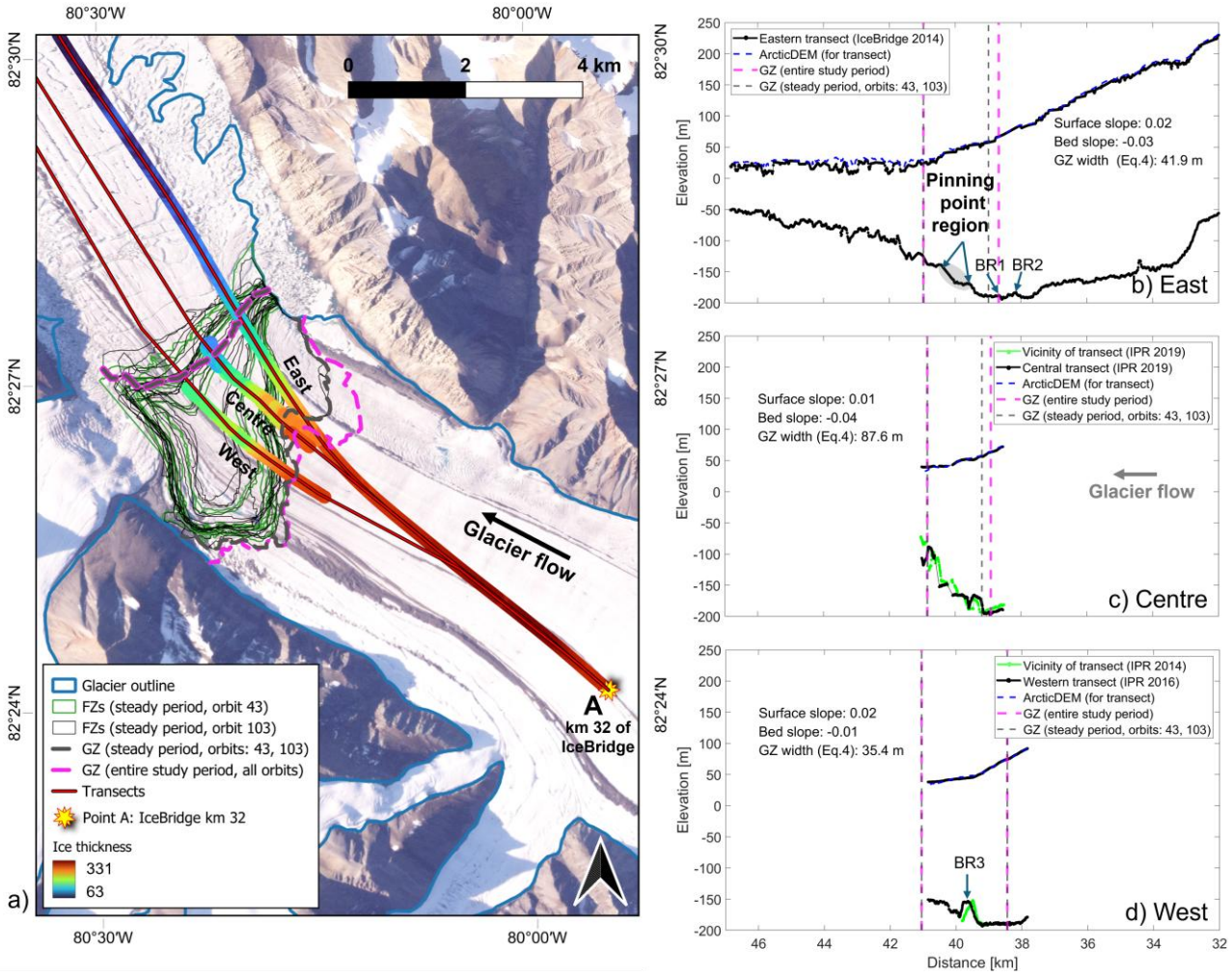


Figure 9: Retrograde bed and surface geometry of the Milne Glacier grounding zone. a) Grounding zones over the steady period (dark grey dashed lines) and the entire study period (magenta dashed lines). The steady period grounding zone is based on the most reliable flexure-zone delineations (uncertainty of ±8 m) from orbits 43 (green) and 103 (black) overlaying the three transects and a Planet image from August 12, 2024 (Image © [2024] Planet Labs PBC). Surface and bed geometry retrieved from the IceBridge and field IPR observations and Arctic DEM along and in vicinity of b) eastern, c) central, d) and western transects. The calculated width of the grounding zone (displayed in text) is about 22 to 74 times smaller than the DDInSAR-derived grounding zone, over entire study period.

To provide context for the observed grounding-zone and flexure-zone widths with respect to changes in glacier velocities, and to allow direct comparison with previously reported annual velocities (Millan et al., 2017; Van Wychen et al., 2020), we present velocities in annual notation in Fig. 10. Over the period of our SAR observations, the Milne Glacier flexure zone was associated with velocities of up to 270 m yr^{-1} during the summer (Fig. 10). The grounded ice moved downstream at about 100 m yr^{-1} and then accelerated to 200 m yr^{-1} at ~3 km up-glacier of the flexure zone, reaching a velocity of 270 m yr^{-1} in the

flexure zone and then up to 320 m yr^{-1} down-glacier of it during summer months. Hence, Milne Glacier flexure zone was
585 associated with up to ~2.7-fold increase of glacier velocity compared against its up-glacier grounded part shown in Fig. 10.

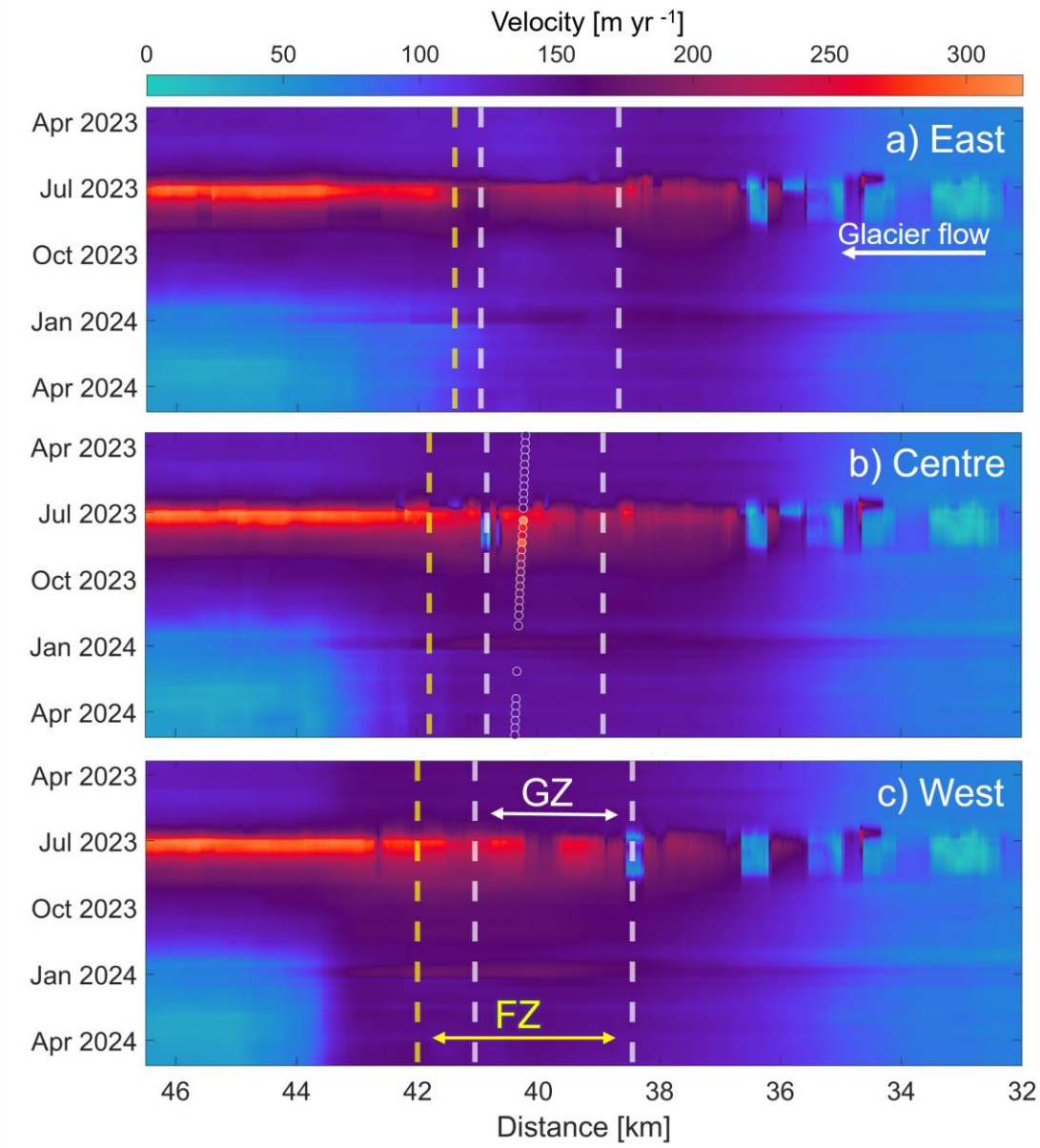


Figure 10: Hovmöller diagram of SAR-derived Milne Glacier velocity along the a) eastern, b) central, and c) western transects with respect to the grounding zone (GZ) and the largest width of the flexure zone (FZ) marked by white and yellow dashed lines
590 **respectively over the observation period. The GNSS locations and associated velocities throughout the observation period are shown as a scatter plot overlaid on the SAR-derived velocities along the central transect. Profiles start at km 32 of the 2014 IceBridge radar transect. (point A in Fig. 1). Velocity fluctuations between km 32 and 37 in the summer are a noise-related artifact.**

The grounding zone, where the grounding line migrated during the observation period, exhibited differences in velocity along the three transects. The widest grounding zone along the western transect of the glacier was associated with the highest velocity of 166.4 m yr^{-1}, averaged over a year and across the observed grounding zone width (Fig. 10 c), and the thickest ice (mean value of 225.6 m, Fig. 9 d). This section discharged approximately 37 540 m^3 yr^{-1} of ice along a 1 m-wide flow line. The narrower and thinner grounding zones along the eastern and central transects, with mean thicknesses of 210.0 m and 200.5 m (Fig. 9 b, c), were associated with slower average velocities of 144.6 m yr^{-1} and 159.8 m yr^{-1} (Fig. 10 a, b), discharged approximately 30 366 m^3 yr^{-1} and 32 040 m^3 yr^{-1} along a 1 m-wide flow line, respectively.

4. Discussion

4.1 Short-term migration of grounding line and changes in the flexure and grounding zones along the transects: SSH and glacier geometry

The intra-annual vertical displacement of the Milne Glacier ice tongue is governed by changes in SSH, which, in turn, are driven by variations in tides and atmospheric pressure. SSH has been identified as a major driving mechanism of grounding-line migration for Thwaites Glacier in West Antarctica (Rignot et al., 2024), Fisher, Mellor, and Lambert glaciers in East Antarctica (Chen et al., 2023), and Jakobshavn Isbræ in Greenland (Kim et al., 2024). These locations have relatively large tidal ranges of about 2-3 m, while other locations, for instance, Rutford Ice Stream in Antarctica, with a tidal range exceeding 7 m, experience even larger tidal forcing (Padman et al., 2018). Atmospheric pressure variability only plays a minor role in the displacement of floating ice shelves and ice tongues in these locations. For marine-terminating glacier systems similar to Milne Glacier, where tidal range is much smaller (< 1 m) than in the aforementioned studies, atmospheric pressure variability plays a more substantial role in controlling SSH, and, consequently, the displacement of the floating ice tongue.

Based on the flexure-zone variables we analyzed, such as distance to the hinge line and flexure-zone width, we found that the grounding line migrates differently along each of the three transects, despite their similar ice thicknesses and exposure to the same water-level changes. These distinct slices of the flexure zones along the three transects could differ due to variations in bed geometry and likely ice stiffness. The width of the flexure zone is governed by ice stiffness, which is determined by ice thickness and the effective Young's modulus (Wild et al., 2017). Our ice-thickness observations revealed only minor differences for the three transects, with thicknesses ranging from 255 to 263 m at the most landward hinge-line position and mean values ranging from 200.5 to 225.6 m within the grounding zone, highlighting the fact that pinning points can further affect the width of the flexure zone. Pinning points act to physically prop up the floating ice tongue, at least at certain water levels, thereby influencing local ice stiffness, ice flexure patterns, and the extent of inland water intrusion with changing tides. In this study, both of the observed pinning points are located near the lateral shear zones, which are associated with reduced ice stiffness (Wild et al., 2025). Previous studies have shown that the presence of pinning points affects lateral and basal shear stresses, generating upstream compression and downstream tension, which, in turn, influences flow variability and can locally

enhance the stiffness of the glacier system and its buttressing (Robel et al., 2017; Still & Hulbe, 2021). In addition, emerging pinning points increase the complexity of the grounding-line shape by forming convex and concave sections, thereby amplifying its sinuosity and further modifying the glacier stress regime (Wild et al., 2018). This can also increase lateral and basal resistance and potentially stabilize the glacier locally. Therefore, the complex interplay between local ice stiffness, grounding line shape, and glacier bed geometry results in the observed flexure-zone widths and governs grounding-line evolution.

Pinning points also control grounding-line migration and, consequently, the width of the grounding zone. Our results support the idea that a wider grounding zone is associated with shallow bed topography, whereas a narrower grounding zone is associated with steeper bed slopes (Milillo et al., 2022; Rignot et al., 2024). The grounding line of Milne Glacier migrates along a retrograde bed slope over tidal cycles forming a distinctive grounding zone along the three transects. The widest grounding zone was observed along the western transect, which has the shallowest bed slope, followed by the eastern transect, and then the central transect, which has the steepest bed slope. The overall bed slope in the grounding zone helps to characterize its width, but local topography also plays an important role. For instance, Chen et al. (2023) used intervals associated with very distinctive bed features for their slope calculations (i.e., an interval within the Lambert Estuary's grounding zone associated with retrograde slope and several intervals up-glacier of Fisher Glacier's grounding zone associated with very steep prograde slopes) to demonstrate a quasi-exponential relationship between grounding-zone width and bed slope. Milne Glacier's topography within its grounding zone controlled the grounding zone width over the period of observations: the newly detected notch, associated with a pinning point, caused a 30% increase in the grounding-zone width along the eastern transect. The grounding-line migration associated with the notch was even more extensive farther east, with landward incursion reaching up to 2.4 km further than the previous grounding zone. Thus, pinning points on retrograde slope inhibit seawater intrusion into bed cavities during low SSH and permit water intrusions farther inland when SSH is high, thereby playing an important role in shaping the flexure zone and positioning the grounding line. Therefore, detailed information on bed geometry up-glacier of the grounding zone is essential for improving predictions of grounding-line retreat, particularly for identifying where potential pinning points may form due to water intrusion and ice ungrounding around bed rises.

4.2 Flexure zone delineation uncertainties during steady and unsteady velocity periods

This study is based on a commonly used DDInSAR approach, which assumes steady glacier flow between paired SAR data acquisitions that form a single interferogram, such that the horizontal component of displacement can be removed through differencing of the two interferograms to reveal the vertical component of displacement due to tidal flexure. We examined the validity of this assumption by quantifying the SAR line-of-sight error caused by velocity variability using available in situ GNSS records. We also assessed SAR line-of-sight error resulting from ice extension and compression due to tidal bending. Analysis of these errors with respect to four RCM orbits with different incidence angles, and both ascending and descending passes - thus different sensitivities to horizontal flow variability - provides insights about the robustness of our DDInSAR

flexure-zone delineations and associated uncertainties. We found that the RCM viewing geometry associated with low incidence angles (between 19º and 30º) and ascending tracks (i.e., orbits 43, 58 and 103) provided the most robust results for the Milne Glacier flexure-zone delineation during the steady period. Particularly, the most reliable flexure zone delineations with ± 8 m uncertainty and high correlation of 0.91 between DDInSAR displacements and DSSH were attributed to orbits 43 and 103. The correlations degraded with increasing changes in velocity, especially for orbit 43.

In contrast, the descending RCM SAR pass (i.e., orbit 09) with a mean incidence angle of 39.5° demonstrated high correlation between DDInSAR and DSSH during both, steady and unsteady periods (0.83 and 0.93, respectively) despite the highest mean LOShV and LOShB errors. This orbit was associated with the highest flexure zone delineation uncertainty of ±222 m resulting from the combined errors due to variable velocity and bending during the unsteady period. This uncertainty would increase if there was an even greater velocity variability. Additionally, larger tidal displacements and thicker ice can increase errors associated with ice extension or compression caused by bending. In particular, the error due to ice bending can be on the order of one ice thickness based on a 1-D model (Rack et al., 2017). This effect may be reduced within embayments and enhanced around protrusions of the grounding line, as suggested by a 2-D model (Wild et al., 2018). Thus, flexure-zone delineations from orbits with high incidence angles, which are sensitive to horizontal surface displacements, should be interpreted with consideration of the associated uncertainties when a glacier experiences substantial velocity variability and/or pronounced tidal bending.

While SAR orbit sensitivity to horizontal displacement due to variable velocity and bending contributes to uncertainty in the current study, understanding and accounting for these horizontal components could also benefit the broader glaciological community. In particular, improved characterization and quantification of the horizontal and vertical displacement contributions to DDInSAR-derived deformation could provide further insights into shear-zone weakening (Wild et al., 2025) and help constrain the neutral depth layer (e.g., Rack et al., 2017; Wild et al., 2018). Furthermore, better constraints on the neutral depth layer could support applications that require more robust estimates of vertical strain within the ice column, such as the assessment of basal melt rates using phase-sensitive radar (Vaňková et al., 2020).

Our investigation was limited by the number of flexure-zone delineations during the unsteady period due to relatively scarce summer SAR observations as well as lack of coherence during the summer season caused by both surface melt and acceleration of the glacier. With the increasing number of SAR observations, larger DDInSAR datasets during the unsteady season can be used along with SAR-derived 2-D velocities (e.g., Samsonov et al., 2021), to further investigate and quantify how the flexure-zone delineation is affected by the SAR viewing geometry with respect to changes in glacier velocity and ice bending across the entire glacier grounding zone.

4.3 Long term grounding-line retreat and bed geometry

The Milne Glacier retrograde bed configuration in the grounding zone allows ocean water to intrude landward with high tides behind two pinning points in its western and eastern margins. This likely enhances ice deterioration far under the glacier which

would promote grounding-line retreat. For instance, Poinelli et al. (2023) suggested that enhanced melt rates around pinning points can lead to the mechanical instability of an ice shelf/tongue. The observed rapid grounding-line retreat in the eastern part of Milne Glacier illustrates the combined effect of bathymetry and ocean forcing. Between 2011 and October of 2023, this part of Milne Glacier was stable and had much narrower grounding zone than western and central parts (Antropova et al., 2024). The eastern grounding zone was also associated with a bed rise on a retrograde slope (before km 41 in Fig. 9 b), which, likely, inhibited the seawater intrusion further inland. As a result of melt processes during summer 2023, the grounding line migrated past the next inland bed rise shown as the landward bound of pinning point region in Fig. 9 b, and the new eastern landward limit of the flexure zone was observed up to 2.4 km up-glacier at 'BR1' in Fig. 9 b. This suggests rapid changes as soon as seawater was able to intrude past the first bed rise, likely driven by the retrograde slope and permanently opened ocean cavities. The eastern transect bathymetry suggests that seawater intrusion further up-glacier is likely currently inhibited by a small bed rise ('BR1' in Fig. 9 b) at km ~38.7 and could be later suppressed by a larger bed rise at km ~38.2 ('BR2' in Fig. 9 b), that will likely become the next landward position for the grounding line. Subsequently, another cavity on a retrograde slope may cause a rapid retreat of the grounding line down to km 37.5, where the bed slope changes to a prograde slope, which should slow down the grounding line's recession.

While tides allow for the renewal of the water inside the cavities around the pinning points, the glacier uplift caused by high tides and low atmospheric pressure also allows periodic seawater intrusions everywhere within the grounding zone. On Petermann Glacier, 400 km southeast of Milne Fiord, Ciraci et al. (2023) estimated that submarine melt rates were up to 80 m/yr in the grounding zone due to seawater intrusions. Sea-water intrusion is also thought to be an important component of the recent retreat of Thwaites Glacier (Rignot et al. 2024) and Jakobshavn Isbræ (Kim et al. 2024). At Milne Fiord, where tidal range is about 0.41 m, a 2.4 km and a 1 km incursion along and across the eastern part of the fjord, respectively, corresponds to approximately 11.4 m^3/s of seawater moving in (during flood tide) or out (during ebb tide) of the Milne Glacier grounding zone. Given that this water is roughly 1°C above the local freezing point at 150 m depth (Hamilton 2021; Bonneau et al., 2024b), these intrusions have the potential to melt ice at a rate of 0.15 m^3/s. This is comparable to the estimated submarine melt rate along the entire ~5 km-wide submerged glacier front, which is 0.82 m^3/s (Bonneau et al., 2024a), underscoring the potential effect of seawater intrusions in Milne Glacier grounding-line retreat.

The grounding zone plays a crucial role in glacier dynamics, as it controls the discharge of ice from the grounded portion of the glacier (Schoof, 2007). The computed average annual velocity along the transects varied from 145 to 166 m yr^{-1} in the grounding zone during the study period, which was close to results (i.e., between 160 and 190 m yr^{-1}) for 1990s reported by Millan et al., (2017) but higher than observed velocities over recent years. The velocity increase observed in the 1990s was followed by the development of the western notch between 1992 and 2011 (Antropova et al., 2024). More recently, between 2010 and 2020, the glacier velocity in the flexure zone ranged from 80 to 160 m yr^{-1} with peak values occurring between 2018 and 2020 (Van Wychen et al., 2020). This study documents further glacier acceleration in the grounding zone, accompanied by the formation of the eastern notch, which was preceded by grounding-line retreat (Antropova et al., 2024). These findings support the idea that Milne Glacier, currently resting on a local retrograde slope within its grounding zone, has likely been

influenced by a positive feedback mechanism in which grounding-line retreat leads to increased ice flux across the grounding line and further ice thinning, which, in turn, promotes additional grounding-line retreat. This process is often referred to as marine ice-sheet instability (MISI), although the classical theory was developed for an unconfined marine ice sheet and ice shelf system rather than for a marine-terminating glacier (Weertman, 1974; Schoof, 2007). Moreover, interactions between ice flow, basal processes, and environmental conditions can alter this mechanism and help stabilize ice sheets (Sergienko and Wingham, 2024) and, more specifically, marine-terminating glaciers (Sergienko, 2022).

The newly observed notch in the eastern part of the glacier might suggest future changes in the glacier dynamics. Our DDInSAR observations of Milne Glacier reveals that its grounding-line retreat along the western and eastern transects were driven by the sea water intrusion upstream of the pinning point, which can lead to a 10%–50% increase in the volume loss from marine-terminating glaciers and ice sheets (Robel et al., 2022). The pronounced Milne Glacier grounding-line retreat between 1992 and 2023 along its western margin started with a notch, which was associated with a pinning point and seawater intrusion behind it (2011 DDInSAR image in Fig. 5 by Antropova et al., 2024). This notch widened towards the glacier centre between 2011 and 2023. The present study shows that the eastern margin has recently also been experiencing an extensive ungrounding around a pinning point, with a new notch likely expanding towards the glacier centre. Thus, the SAR-derived patterns of the grounding-line retreat suggest that ice ungrounding progresses from pinning points towards the glacier centre driving ice deterioration and further grounding-line retreat. Comprehensive in situ observations of ice thinning and melt processes near pinning points combined with detailed bed information and frequent satellite DDInSAR observations would provide additional details and insights about processes causing ice deterioration near the pinning points.

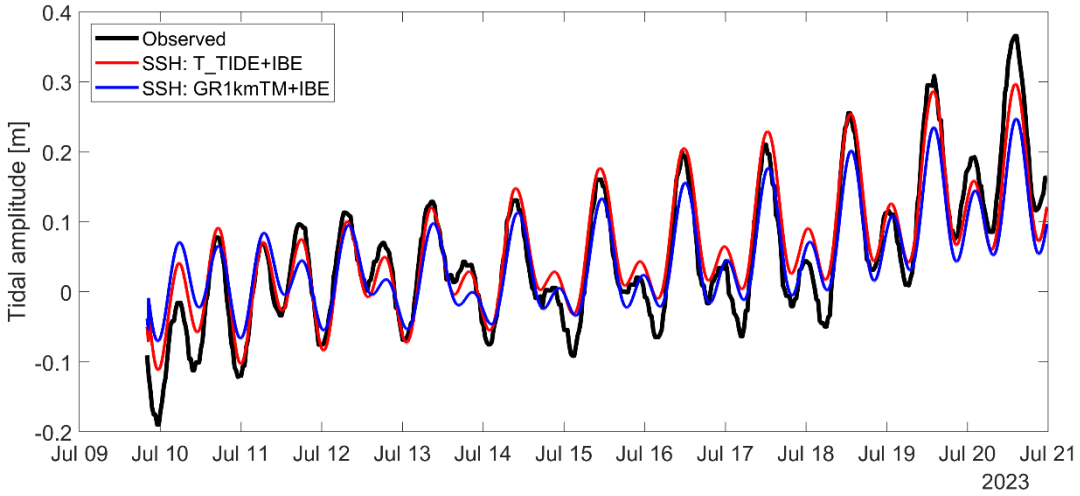
Conclusions

Our study demonstrated the benefits of the RCM 4-day high-resolution coherent change detection acquisition cycle for monitoring of glacier flexure-zones and grounding-line migration at a high temporal resolution from four different orbits. These relatively frequent RCM data acquisitions spanning from February 2023 to September 2024 allowed us to examine a large SAR dataset to better understand the Milne Glacier flexure-zone intra-annual migration pattern, while also taking into account the SAR viewing geometry and quantifying uncertainties associated with glacier velocity variability and ice bending. In addition, we were able to support our DDInSAR observations with in situ glacier-specific and environmental datasets. The most reliable DDInSAR results, with low LOShV (i.e., line-of-sight horizontal component of displacement due to velocity variability) and LOShB (i.e., line-of-sight horizontal component of displacement due to ice bending) errors and associated uncertainties within one pixel, were obtained from orbits with low incidence angles and ascending tracks. The highest uncertainty, approximately 22 pixels, was obtained for an orbit with a high incidence angle and a descending track, which was most sensitive to horizontal ice-surface displacement caused by velocity variability and bending. Our results showed that Milne Glacier flexure-zone intra-annual migration is driven by tidal cycles and atmospheric pressure variability. Bed geometry, specifically pinning points, plays a crucial role in shaping the flexure zone and governing grounding-line retreat. In situ

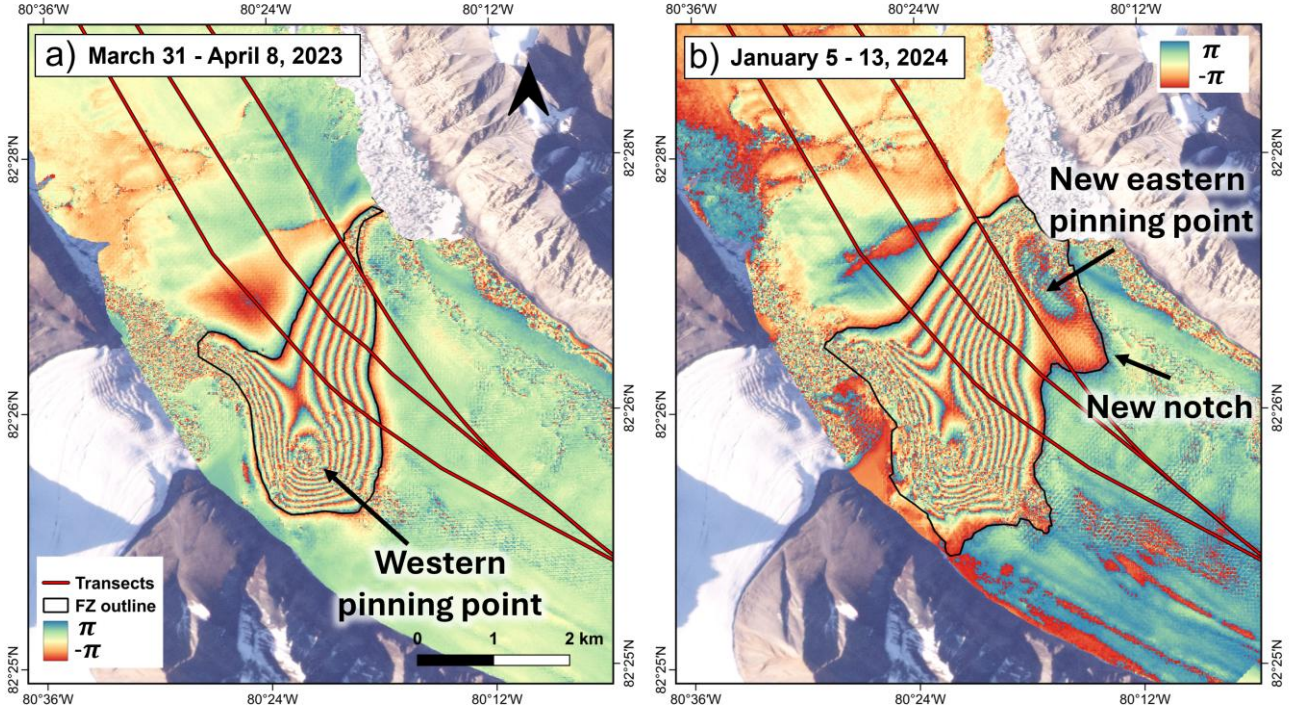
observations of melt processes near pinning points could provide further insight into their influence on grounding-line dynamics.

Continuous frequent satellite-based monitoring of changes in the flexure zone of marine-terminating glaciers, as demonstrated in the present study using RCM SAR, serves as an efficient tool to explore short-term migration of these crucial zones. Consistent and frequent SAR observations over Arctic and Antarctic glaciers in combination with improved datasets on their bed geometry and ice thinning will ultimately improve our understanding of ice deterioration in the grounding zone and its future evolution. In particular, detailed bed geometry upstream of the grounding zone, in regions that may become marine in the future, is key information required to improve glacier modeling capabilities and predictions.

Appendix A



765 **Figure A1: Observed tides measured in situ with a moored pressure sensor in July 2023 (black) and computed sea surface heights (SSH) using IBE-corrected T_TIDE simulations (red) and the Gr1kmTM model (blue) (Howard and Padman, 2021). IBE was calculated based on GEM model pressure records. The correlation between the observed and computed SSH is 0.96 for T_TIDE and 0.93 for Gr1kmTM, with RMSE values of 3.4 cm and 4.6 cm, respectively.**



770 **Figure A2: DDInSAR image examples from orbit 103 showing: a) the flexure zone without the eastern notch, b) the flexure zone with the newly formed notch around the eastern pinning point.**

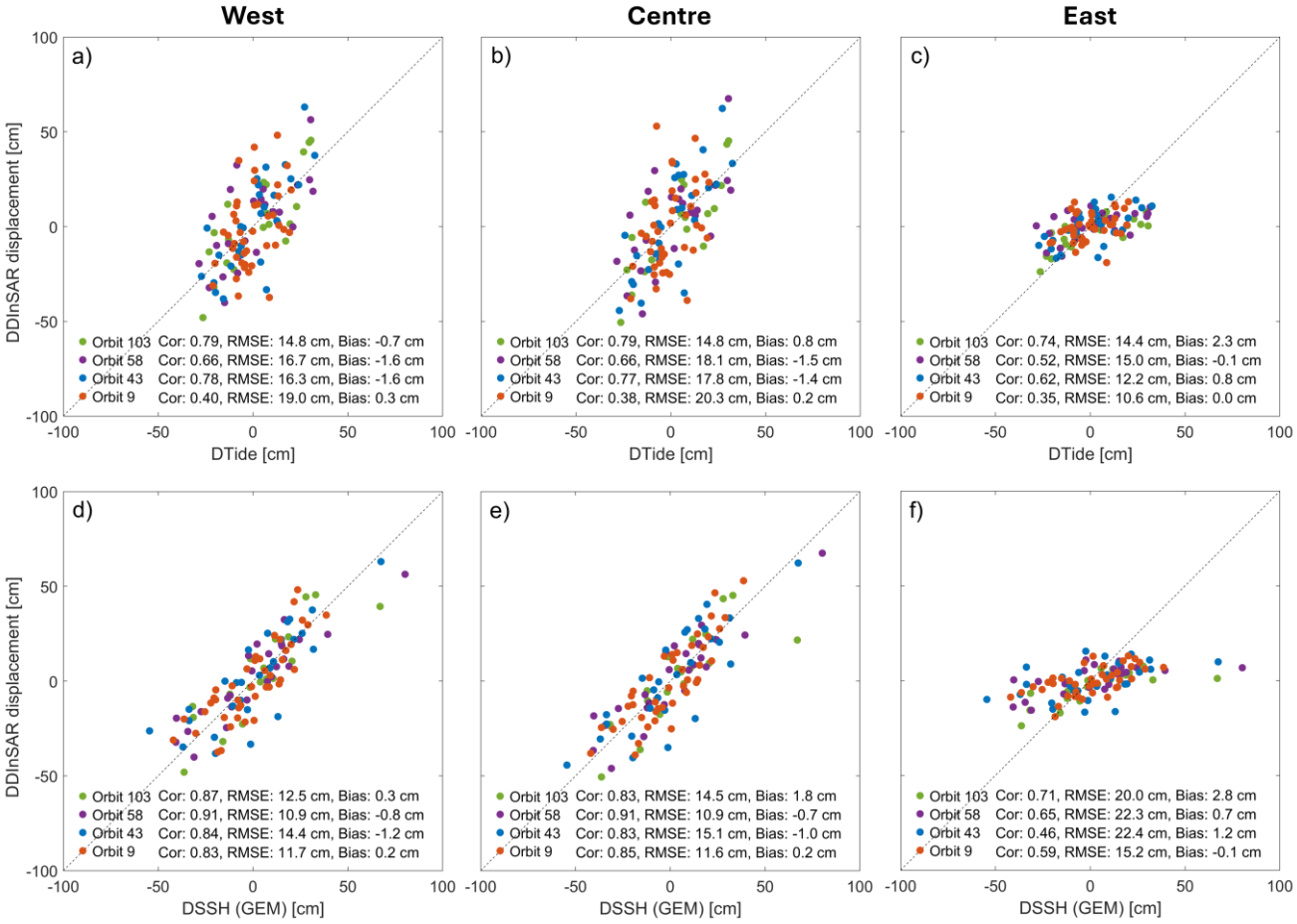


Figure A3: Relationship results for the three transects. Upper panels: relationships between DDInSAR displacement and differential displacement of simulated tides (DTide) without IBE for the: a) western, b) central, and c) eastern transects. Lower panels: relationships between DDInSAR displacement and differential displacement of sea surface height (DSSH) based on Global Environmental Multiscale (GEM) model for the: d) western, e) central, and f) eastern transects. The different orbits are denoted by coloured symbols. 'Cor' - the Pearson correlation coefficient, 'RMSE' - Root mean square error, the 1:1 is plotted as a dashed line.

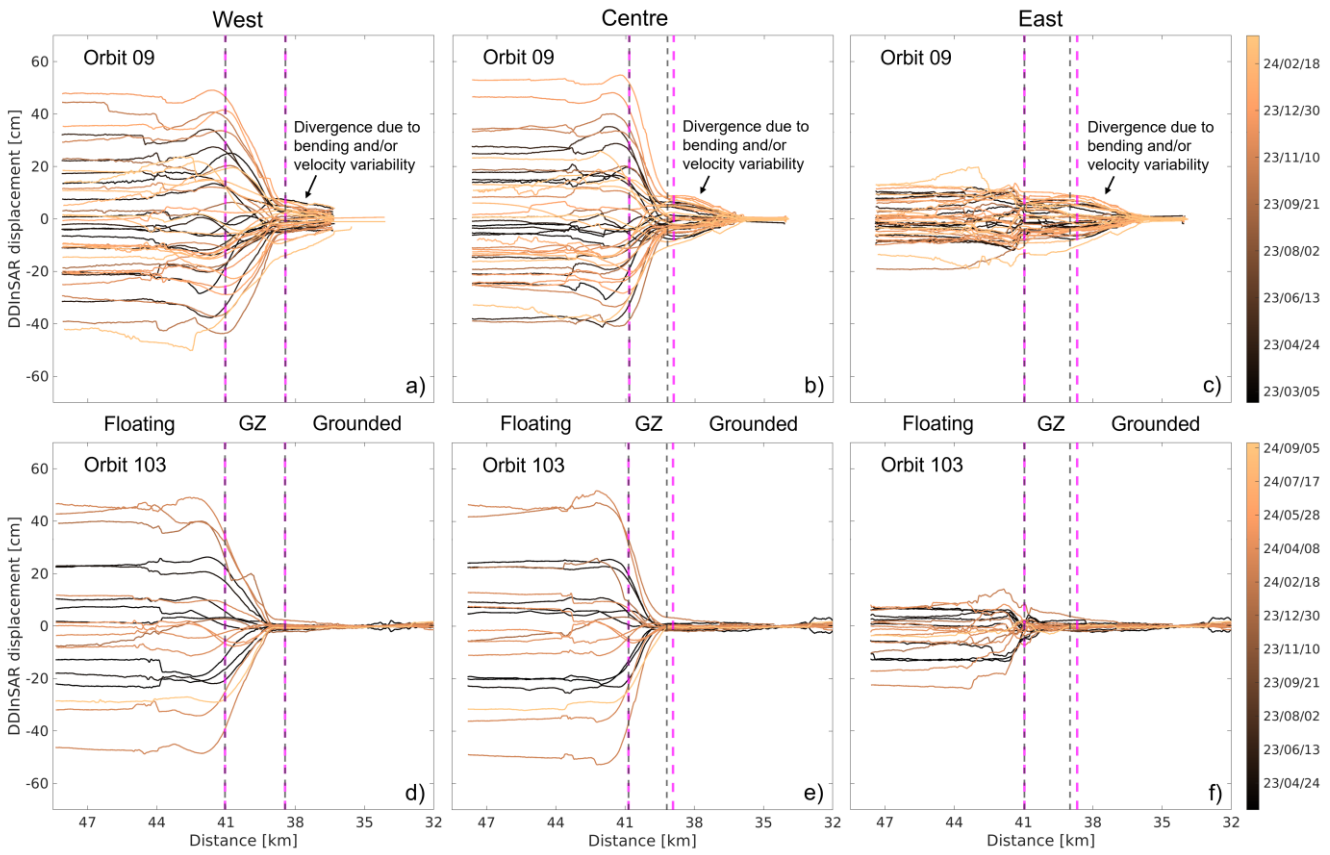


Figure A4: DDInSAR-derived curves of surface displacement from Orbit 09 along the a) western, b) central, and c) eastern transects and from Orbit 103 along the d) western, e) central, and f) eastern transects, starting at km 32 of the 2014 IceBridge radar profile (i.e., point A in Fig. 1). Grounding zones (GZ) during the steady period and over the entire study period are shown as dark grey and magenta vertical dashed lines, respectively. The line-of-sight mean errors due to tidal bending and velocity variability for Orbit 09 were high (Fig. 7a, b), resulting in divergence of the curves from zero upstream of the grounding zone. In contrast, Orbit 103 demonstrated negligible line-of-sight mean errors due to tidal bending and velocity variability, with minimal deflection of the curves from zero upstream of the grounding zone. The delineated grounding zone was not substantially affected by the curve deflections observed for Orbit 09.

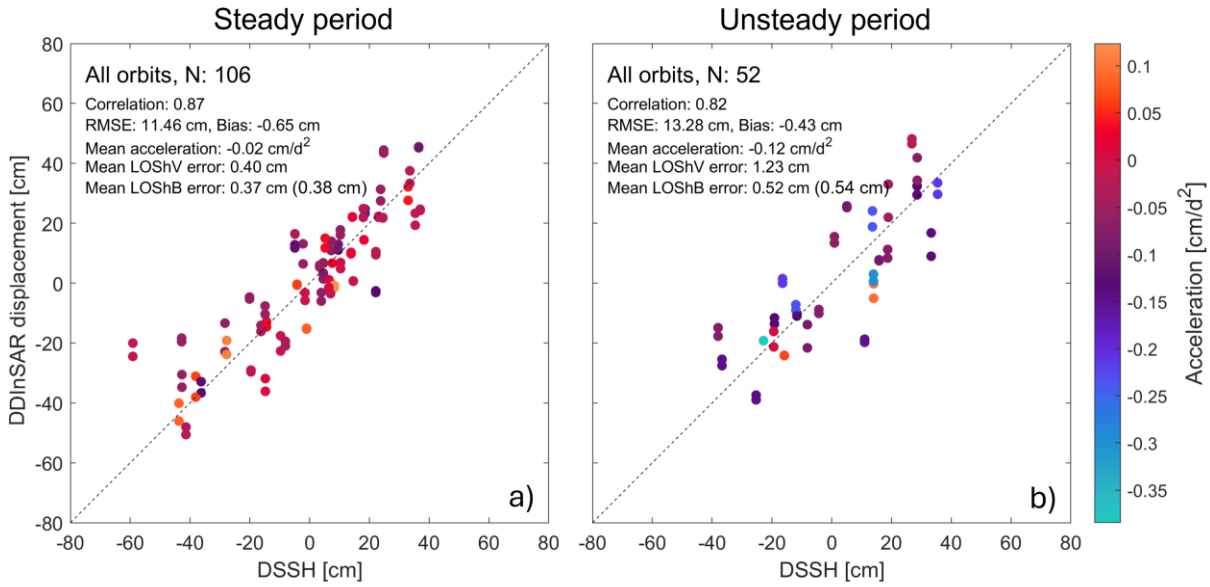


Figure A5: DDInSAR-derived displacements versus DSSH combined along the western and central transects with respect to the two glacier velocity periods. a) Steady period with minimal changes in velocities and b) Unsteady period with more pronounced changes in velocities as defined in Fig. 2. LOShV represents error due to variable velocity based on in situ GNSS records, and LOShB represents error due to ice surface extension or compression from tidal bending along the central (western) transect.

Appendix B

We assume that the glacier vertical displacement can be described by the multi-frequency harmonic function given by Eq. 1. Determining all the coefficients at once represents an ill-posed problem that requires regularization, but the resulting solution was still found to be unstable exhibiting high-frequency fluctuations. To achieve a more stable solution, instead of deriving all the coefficients at once, we chose to derive the coefficients sequentially starting with the frequency corresponding to the most dominant tidal constituent (j=1) and finishing with the frequency corresponding to the least dominant tidal constituent (j=N).

First, we determined the coefficients corresponding to the dominant semidiurnal M2 tidal constituent (j=1). Each observed SAR-derived double difference displacement, Δd_i (i is the number of observations: 1, 2, … n) is given by the following linear combination with unknown coefficients a_j, b_j, and c_j:

$$\Delta d_i = a_j S_i + b_j C_i + c_j H_i, \tag{B1}$$

where

$$S_i = [\sin(\omega_j t_2^{(i)}) - \sin(\omega_j t_1^{(i)})] - [\sin(\omega_j t_4^{(i)}) - \sin(\omega_j t_3^{(i)})], \tag{B2}$$

$$C_i = [\cos(\omega_j t_2^{(i)}) - \cos(\omega_j t_1^{(i)})] - [\cos(\omega_j t_4^{(i)}) - \cos(\omega_j t_3^{(i)})], \tag{B3}$$

$$H_i = [H(t_2^{(i)}) - H(t_1^{(i)})] - [H(t_4^{(i)}) - H(t_3^{(i)})], \tag{B4}$$

where $t_j^{(i)}$ are known times of RCM SAR data acquisitions represented as serial date numbers (e.g., the MATLAB notation of 'datenum') and ω_j is the circular frequency corresponding to the j^{th} tidal constituent.

For the set of n DDInSAR observations, the following system of linear equations can be obtained:

$$MA = D, \tag{B5}$$

where:

$$M = \begin{bmatrix} S_1 & C_1 & H_1 \\ S_2 & C_2 & H_2 \\ \cdots & \cdots & \cdots \\ S_n & C_n & H_n \end{bmatrix}, D = \begin{bmatrix} \Delta d_1 \\ \Delta d_2 \\ \cdots \\ \Delta d_n \end{bmatrix}, A = \begin{bmatrix} a_j \\ b_j \\ c_j \end{bmatrix}.. \tag{B6}$$

Then, the unknown coefficients A can be derived using Tikhonov's regularization approach as follows:

$$A = (M^T M + \lambda^2 I)^{-1} M^T D, \tag{B7}$$

where I is the identity 3×3 matrix, and λ is the regularization parameter. We note that for the dominant frequency ($j = 1$) the least-square problem is well-posed, so the regularization is not required (i.e., $\lambda = 0$), but for the other frequencies ($j > 1$) regularization must be applied, and λ was chosen to be 3.6 based on the L-curve analysis (Fig. B1 a).

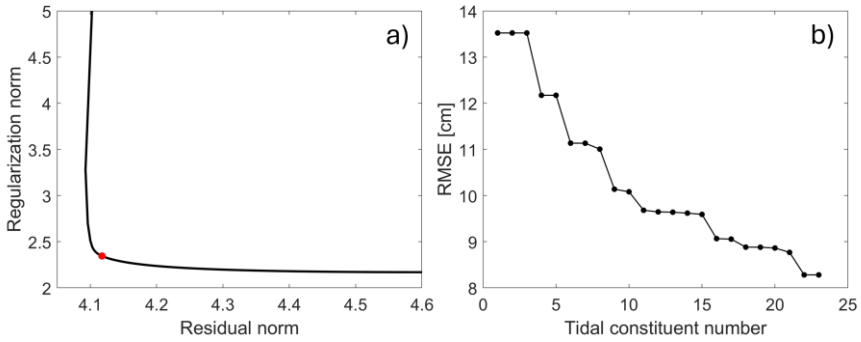


Figure B1: Ice-surface reconstruction parameter analysis. a) L-curve analysis results, with the red dot indicating the optimal regularization parameter, λ = 3.6. b) RMSE versus the number of included constituents.

Once A is found for the first frequency ($j = 1$), D can be updated as $D \leftarrow D - MA$, and the process from (B1) to (B7) is repeated. By running the same approach for the other frequencies $j = 2..N$, all the coefficients a_j and b_j can be determined. The final solution for coefficient $c = \sum_{j=1}^{N} c_j$.

Data availability: The authors do not have permission to share raw RCM data, but it can be accessed by registering a vetted user account (https://www.asc-csa.gc.ca/eng/satellites/radarsat/access-to-data/about.asp). InSAR results, as well as other field, simulated, and modeled data used in this study, are available upon request. The IceBridge airborne radar data (IceBridge MCoRDS L2 Ice Thickness, Version 1 [IRMCR2_20140401_03], https://doi.org/10.5067/GDQ0CUCVTE2Q) are freely available at https://nsidc.org/data/irmcr2/versions/1.

Author contribution: YA: collected field data, developed methodology and algorithms to conduct the data processing and analysis, participated in the funding acquisition, prepared the initial manuscript; DM: supervised the research project, acquired funding, managed field work, collected data; SS: developed software and conducted SAR data processing; AK: tasked RCM satellites, participated in the data analysis; JB: collected and processed field data. All: conceptualized the research project, reviewed, and edited the manuscript.

Competing interests: The authors declare that they have no conflict of interest.

Acknowledgements: We are thankful to the Polar Continental Shelf Program for the logistical support that greatly facilitated all field work activities related to this study, and to the Research Computing Services at Carleton University for IT support. We thank all members of the 2014, 2016, 2019, 2022, and 2023 field campaigns in Milne Fiord. We are grateful to Adam Garbo for building the GNSS instruments. We thank the Canadian Space Agency for providing the RADARSAT Constellation Mission (RCM) imagery. The airborne radar data used in this study were acquired by NASA's Operation IceBridge (Paden et al., 2019; https://doi.org/10.5067/GDQ0CUCVTE2Q). We acknowledge the use of data products from CReSIS generated with support from the University of Kansas, NSF grant ANT- 0424589, and NASA Operation IceBridge grant NNX16AH54G. We thank Ian Delaney for editorial handling, and Christian T. Wild, the anonymous reviewer, and Sam Herreid for reviewing our manuscript and providing valuable and insightful feedback.

Financial support: This project was supported by the: Natural Sciences and Engineering Research Council of Canada (YA: CGS M 2019, and PGSD3–546559-2020; DM: Discovery Grant and Northern Research Supplement RGPIN-2016-06244, RGPNS-2022-04875), W. Garfield Weston Foundation (YA: 2019–2020 Northern Research and Extended Stay Awards), Canada Foundation for Innovation (DM:31410), Ontario Research Foundation (DM: 31410), Polar Continental Shelf Program (DM: 627–18; 651-14, 636-16, 651–19, 665-22, 655–23), ArcticNet (a Network of Centres of Excellence of Canada) GO-Ice project (YA,DM, and JB), Polar Knowledge Canada (YA and JB: Northern Scientific Training Program 2019, 2022, and 2023).

References

Antropova, Y. K., Mueller, D., Samsonov, S. V., Komarov, A. S., Bonneau, J., and Crawford, A. J.: Grounding-line retreat of Milne Glacier, Ellesmere Island, Canada over 1966–2023 from satellite, airborne, and ground radar data, *Remote Sens. Environ.*, **315**, 114478, https://doi.org/10.1016/j.rse.2024.114478, 2024.

Black, T. E. and Joughin, I.: Multi-decadal retreat of marine-terminating outlet glaciers in northwest and central-west Greenland, *The Cryosphere*, **16**, 807–824, https://doi.org/10.5194/tc-16-807-2022, 2022.

Bonneau, J., Laval, B. E., Mueller, D., Hamilton, A. K., and Crawford, A. J.: Heat fluxes in a glacial fjord: the role of buoyancy-driven circulation and offshore forcing, *Geophys. Res. Lett.*, https://doi.org/10.1029/2024GL111242, 2024a.

Bonneau, J., Laval, B. E., Mueller, D., Hamilton, A. K., and Forrest, A. L.: Unsteady circulation in a glacial fjord: a multiyear modeling study of Milne Fiord, *J. Geophys. Res. Oceans*, **129**, e2023JC020140, https://doi.org/10.1029/2023JC020140, 2024b.

Buehner, M., McTaggart-Cowan, R., Beaulne, A., Charette, C., Garand, L., Heilliette, S., Lapalme, E., Laroche, S., Macpherson, S. R., Morneau, J., and Zadra, A.: Implementation of deterministic weather forecasting systems based on ensemble–variational data assimilation at Environment Canada. Part I: The global system, *Mon. Weather Rev.*, https://doi.org/10.1175/MWR-D-14-00354.1, 2015.

Carnahan, E., Catania, G., and Bartholomaus, T. C.: Observed mechanism for sustained glacier retreat and acceleration in response to ocean warming around Greenland, *The Cryosphere*, **16**, 4305–4317, https://doi.org/10.5194/tc-16-4305-2022, 2022.

Chartrand, A. M., Howat, I. M., Joughin, I. R., and Smith, B. E.: Thwaites Glacier thins and retreats fastest where ice-shelf channels intersect its grounding zone, *The Cryosphere*, **18**, 4971–4992, https://doi.org/10.5194/tc-18-4971-2024, 2024.

Chen, H., Rignot, E., Scheuchl, B., and Ehrenfeucht, S.: Grounding zone of Amery Ice Shelf, Antarctica, from differential synthetic-aperture radar interferometry, *Geophys. Res. Lett.*, **50**, e2022GL102430, https://doi.org/10.1029/2022GL102430, 2023.

Ciracì, E., Rignot, E., Scheuchl, B., Tolpekin, V., Wollersheim, M., An, L., Milillo, P., Bueso-Bello, J.-L., Rizzoli, P., and Dini, L.: Melt rates in the kilometer-size grounding zone of Petermann Glacier, Greenland, before and during a retreat, *Proc. Natl. Acad. Sci. USA*, **120**, e2220924120, https://doi.org/10.1073/pnas.2220924120, 2023.

CReSIS: 2014 Greenland P3 data, digital media, Lawrence, Kansas, USA, available at: http://data.cresis.ku.edu/, 2021.

Costantini, M.: A novel phase unwrapping method based on network programming, *IEEE Trans. Geosci. Remote Sens.*, **36**, 813–821, https://doi.org/10.1109/36.673674, 1998.

Freer, B. I. D., Marsh, O. J., Hogg, A. E., Fricker, H. A., and Padman, L.: Modes of Antarctic tidal grounding line migration revealed by ICESat-2 laser altimetry, *The Cryosphere*, **17**, 4079–4101, https://doi.org/10.5194/tc-17-4079-2023, 2023.

Fricker, H. A., Coleman, R., Padman, L., Scambos, T. A., Bohlander, J., and Brunt, K. M.: Mapping the grounding zone of the Amery Ice Shelf, East Antarctica using InSAR, MODIS and ICESat, *Antarct. Sci.*, **21**, 515–532, https://doi.org/10.1017/S095410200999023X, 2009.

Garbo, A.: Cryologger glacier velocity tracker (v2.3.1) [software], available at: https://github.com/cryologger/glacier-velocity-tracker, 2024.

Hamilton, A. K., Mueller, D., and Laval, B. E.: Ocean modification and seasonality in a northern Ellesmere Island glacial fjord prior to ice shelf breakup: Milne Fiord, *J. Geophys. Res. Oceans*, **126**, e2020JC016975, https://doi.org/10.1029/2020JC016975, 2021.

Han, H. and Lee, H.: Tide deflection of Campbell Glacier Tongue, Antarctica, analyzed by double-differential SAR interferometry and finite element method, Remote Sens. Environ., 141, 201–213, https://doi.org/10.1016/j.rse.2013.11.002, 2014.

Hansen, P. C.: Analysis of discrete ill-posed problems by means of the L-curve, SIAM Rev., 34, 561–580, https://doi.org/10.1137/1034115, 1992.

Holmes, F. A., Barnett, J., Åkesson, H., Morlighem, M., Nilsson, J., Kirchner, N., and Jakobsson, M.: Sea level rise contribution from Ryder Glacier in northern Greenland varies by an order of magnitude by 2300 depending on future emissions, *The Cryosphere*, **19**, 2695–2714, https://doi.org/10.5194/tc-19-2695-2025, 2025.

Howard, S. L. and Padman, L.: Gr1kmTM: Greenland 1 kilometer tide model, Arctic Data Center, https://doi.org/10.18739/A2251FM3S, 2021.

Hu, J., Li, Z. W., Ding, X. L., Zhu, J. J., Zhang, L., and Sun, Q.: Resolving three-dimensional surface displacements from InSAR measurements: a review, *Earth-Sci. Rev.*, **133**, 1–17, https://doi.org/10.1016/j.earscirev.2014.02.005, 2014.

Jeffries, M. O.: Milne Glacier, northern Ellesmere Island, NWT, Canada: a surging glacier?, *J. Glaciol.*, **30**, 251–253, 1984.

Kochtitzky, W. and Copland, L.: Retreat of Northern Hemisphere marine-terminating glaciers, 2000–2020, *Geophys. Res. Lett.*, **49**, e2021GL096501, https://doi.org/10.1029/2021GL096501, 2022.

Kim, J. H., Rignot, E., Holland, D., and Holland, D. M.: Seawater intrusion at the grounding line of Jakobshavn Isbræ, Greenland, from terrestrial radar interferometry, *Geophys. Res. Lett.*, **51**, e2023GL106181, https://doi.org/10.1029/2023GL106181, 2024.

MDA Space: RADARSAT Constellation Mission product specification, available at: https://download-telecharger.services.geo.ca/..., 2021.

Millan, R., Jager, E., Mouginot, J., Wood, M. H., Larsen, S. H., Mathiot, P., Jourdain, N. C., and Bjørk, A.: Rapid disintegration and weakening of ice shelves in North Greenland, *Nat. Commun.*, **14**, 6914, https://doi.org/10.1038/s41467-023-42198-2, 2023.

Millan, R., Mouginot, J., and Rignot, E.: Mass budget of the glaciers and ice caps of the Queen Elizabeth Islands, Canada, from 1991 to 2015, *Environ. Res. Lett.*, **12**, 024016, https://doi.org/10.1088/1748-9326/aa5b04, 2017.

Milillo, P., Rignot, E., Mouginot, J., Scheuchl, B., Morlighem, M., Li, X., and Salzer, J. T.: Short-term grounding zone dynamics of Pine Island Glacier, *Geophys. Res. Lett.*, **44**, 10436–10444, https://doi.org/10.1002/2017GL074320, 2017.

Milillo, P., Rignot, E., Rizzoli, P., Scheuchl, B., Mouginot, J., Bueso-Bello, J. L., Prats-Iraola, P., and Dini, L.: Rapid glacier retreat rates observed in West Antarctica, *Nat. Geosci.*, **15**, 51–56, https://doi.org/10.1038/s41561-021-00877-z, 2022.

Mohajerani, Y., Jeong, S., Scheuchl, B., Velicogna, I., Rignot, E., and Milillo, P.: Automatic delineation of glacier grounding lines using deep learning, *Sci. Rep.*, **11**, 1–13, https://doi.org/10.1038/s41598-021-84309-3, 2021.

Morlighem, M., Wood, M., Seroussi, H., Choi, Y., and Rignot, E.: Modeling the response of northwest Greenland to enhanced ocean thermal forcing, *The Cryosphere*, **13**, 723–734, https://doi.org/10.5194/tc-13-723-2019, 2019.

Mortimer, C. A., Copland, L., and Mueller, D. R.: Volume and area changes of the Milne Ice Shelf, Ellesmere Island, Nunavut, Canada, since 1950, *J. Geophys. Res. Earth Surf.*, **117**, https://doi.org/10.1029/2011JF002074, 2012.

Mueller, D., Copland, L., and Jeffries, M. O.: Changes in Canadian Arctic ice shelf extent since 1906, in: *Arctic Ice Shelves and Ice Islands*, 109–148, https://doi.org/10.1007/978-94-024-1101-0_5, 2017.

Natural Resources Canada (NRCan): Canadian Spatial Reference System precise point positioning (CSRS-PPP) service, available at: https://webapp.csrs-scrs.nrcan-rncan.gc.ca/geod/tools-outils/ppp.php, 2024.

Paden, J., Li, J., Leuschen, C., Rodriguez-Morales, F., and Hale, R.: IceBridge MCoRDS L2 ice thickness, Version 1, NASA National Snow and Ice Data Center Distributed Active Archive Center, https://doi.org/10.5067/GDQ0CUCVTE2Q, 2019.

Padman, L., Siegfried, M. R., and Fricker, H. A.: Ocean Tide Influences on the Antarctic and Greenland Ice Sheets, Rev. Geophys., 56, 142–184, https://doi.org/10.1002/2016RG000546, 2018.Padman, L., King, M., Goring, D., Corr, H., and Coleman, R.: Ice-shelf elevation changes due to atmospheric pressure variations, *J. Glaciol.*, **49**, 521–526, https://doi.org/10.3189/172756503781830386, 2003.

Pawlowicz, R., Beardsley, B., and Lentz, S.: Classical tidal harmonic analysis including error estimates in MATLAB using T_TIDE, *Comput. Geosci.*, **28**, 929–937, https://doi.org/10.1016/S0098-3004(02)00013-4, 2002.

Planet Team: Planet application program interface: in space for life on Earth, San Francisco, CA, available at: https://api.planet.com/, 2024.

Poinelli, M., Nakayama, Y., Larour, E., Vizcaino, M., and Riva, R.: Ice-front retreat controls on ocean dynamics under Larsen C Ice Shelf, Antarctica, *Geophys. Res. Lett.*, **50**, e2023GL104588, https://doi.org/10.1029/2023GL104588, 2023.

Porter, C., Howat, I., Noh, M.-J., Husby, E. Khuvis, S., Danish, E., Tomko, K., Gardiner, J., Negrete, A., Yadav, B., Klassen, J., Kelleher, C., Cloutier, M., Bakker, J., Enos, J., Arnold, G., Bauer, G., Morin, P: "ArcticDEM - Mosaics, Version 4.1", https://doi.org/10.7910/DVN/3VDC4W, Harvard Dataverse, V1, 2023.

Rack, W., King, M. A., Marsh, O. J., Wild, C. T., and Floricioiu, D.: Analysis of ice shelf flexure and its InSAR representation in the grounding zone of the southern McMurdo Ice Shelf, The Cryosphere, 11, 2481–2490, https://doi.org/10.5194/tc-11-2481-2017, 2017.

Ramanath, S., Krieger, L., Floricioiu, D., Diaconu, C.-A., and Heidler, K.: Automatic grounding line delineation of DInSAR interferograms using deep learning, The Cryosphere, 19, 2431–2455, https://doi.org/10.5194/tc-19-2431-2025, 2025.

Rantanen, M., Karpechko, A. Y., Lipponen, A., Nordling, K., Hyvärinen, O., Ruosteenoja, K., Vihma, T., and Laaksonen, A.: The Arctic has warmed nearly four times faster than the globe since 1979, *Commun. Earth Environ.*, **3**, 168, https://doi.org/10.1038/s43247-022-00498-3, 2022.

Rignot, E., Ciracì, E., Scheuchl, B., Tolpekin, V., Wollersheim, M., and Dow, C.: Widespread seawater intrusions beneath the grounded ice of Thwaites Glacier, West Antarctica, *Proc. Natl. Acad. Sci. USA*, **121**, e2404766121, https://doi.org/10.1073/pnas.2404766121, 2024.

Rignot, E.: Tidal motion, ice velocity and melt rate of Petermann Gletscher, Greenland, measured from radar interferometry, *J. Glaciol.*, **42**, 476–485, https://doi.org/10.3189/S0022143000003464, 1996.

Robel, A. A., Tsai, V. C., Minchew, B., and Simons, M.: Tidal modulation of ice shelf buttressing stresses, Ann. Glaciol., 58, 12–20, https://doi.org/10.1017/aog.2017.22, 2017.

Robel, A. A., Wilson, E., and Seroussi, H.: Layered seawater intrusion and melt under grounded ice, *The Cryosphere*, **16**, 451–469, https://doi.org/10.5194/tc-16-451-2022, 2022.

Rocca, F., Prati, C., and Ferretti, A.: Space-borne SARs: impact of wavelengths and scan modes on ground motion studies, *Ann. GIS*, **16**, 69–79, https://doi.org/10.1080/19475683.2010.492124, 2010.

Samsonov, S.: Multidimensional small baseline subset (MSBAS) software for constrained and unconstrained deformation analysis, *Can. J. Remote Sens.*, **50**, 2424753, https://doi.org/10.1080/07038992.2024.2424753, 2024.

Samsonov, S., Tiampo, K., and Cassotto, R.: Measuring the state and temporal evolution of glaciers in Alaska and Yukon using SAR-derived 3D time series, *The Cryosphere*, **15**, 4221–4239, https://doi.org/10.5194/tc-15-4221-2021, 2021.

Schoof, C.: Ice sheet grounding line dynamics: steady states, stability, and hysteresis, *J. Geophys. Res. Earth Surf.*, **112**, https://doi.org/10.1029/2006JF000664, 2007.

Sergienko, O. V.: Marine outlet glacier dynamics, steady states and steady-state stability, J. Glaciol., 68, 946–960, https://doi.org/10.1017/jog.2022.13, 2022.

Sergienko, O. and Wingham, D. J.: Diverse behaviors of marine ice sheets in response to temporal variability of the atmospheric and basal conditions, J. Glaciol., 70, e52, 1–12, https://doi.org/10.1017/jog.2024.43, 2024.Still, H. and Hulbe, C.: Mechanics and dynamics of pinning points on the Shirase Coast, West Antarctica, The Cryosphere, 15, 2647–2665, https://doi.org/10.5194/tc-15-2647-2021, 2021.

Tsai, V. C. and Gudmundsson, G. H.: An improved model for tidally modulated grounding-line migration, *J. Glaciol.*, **61**, 216–222, https://doi.org/10.3189/2015JoG14J152, 2015.

Vaňková, I., Nicholls, K. W., Corr, H. F. J., Makinson, K., and Brennan, P. V.: Observations of tidal melt and vertical strain at the Filchner-Ronne Ice Shelf, Antarctica, J. Geophys. Res.-Earth Surf., 125, e2019JF005280, https://doi.org/10.1029/2019JF005280, 2020.

Van Wychen, W. V., Burgess, D., Kochtitzky, W., Nikolic, N., Copland, L., and Gray, L.: RADARSAT-2-derived glacier velocities and dynamic discharge estimates for the Canadian High Arctic, *Can. J. Remote Sens.*, **46**, 695–714, https://doi.org/10.1080/07038992.2020.1859359, 2020.

Veillette, J., Mueller, D. R., Antoniades, D., and Vincent, W. F.: Arctic epishelf lakes as sentinel ecosystems: past, present and future, *J. Geophys. Res. Biogeosci.*, **113**, 2008.

Werner, C., Wegmüller, U., Strozzi, T., and Wiesmann, A.: GAMMA SAR and interferometric processing software, in: *ERS–ENVISAT Symposium*, Gothenburg, Sweden, 16–20, 2000.

Weertman, J.: Stability of the junction of an ice sheet and an ice shelf, J. Glaciol., 13, 3–11, https://doi.org/10.3189/S0022143000023327, 1974.

Wild, C. T., Drews, R., Neckel, N., Lee, J., Kim, S., Han, H., Lee, W. S., Helm, V., Rosier, S. H. R., Marsh, O. J., and Rack, W.: Monitoring shear-zone weakening in East Antarctic outlet glaciers through differential InSAR measurements, *The Cryosphere*, **19**, 4533–4554, https://doi.org/10.5194/tc-19-4533-2025, 2025.

Wild, C. T., Marsh, O. J., and Rack, W.: Differential interferometric synthetic aperture radar for tide modelling in Antarctic ice-shelf grounding zones, The Cryosphere, 13, 3171–3191, https://doi.org/10.5194/tc-13-3171-2019, 2019.

Wild, C. T., Marsh, O. J., and Rack, W.: Unraveling InSAR-observed Antarctic ice-shelf flexure using 2-D elastic and viscoelastic modeling, *Front. Earth Sci.*, **6**, https://doi.org/10.3389/feart.2018.00028, 2018.

Wild, C. T., Marsh, O. J., and Rack, W.: Viscosity and elasticity: a model intercomparison of ice-shelf bending in an Antarctic grounding zone, *J. Glaciol.*, **63**, 573–580, https://doi.org/10.1017/jog.2017.15, 2017.

Wunsch, C. and Stammer, D.: Atmospheric loading and the oceanic “inverted barometer” effect, *Rev. Geophys.*, **35**, 79–107, https://doi.org/10.1029/96RG03037, 1997.